Wetting at nanoscale: Effect of surface forces and droplet size

Nikolai Kubochkin [*] and Tatiana Gambaryan-Roisman
Institute for Technical Thermodynamics, Technische Universität Darmstadt,
Alarich-Weiss-Straße 10, 64287, Darmstadt, Germany

Despite being intensively investigated, wetting at the nanoscale leaves a manifold of questions unresolved. In particular, the dependence of a contact angle on a droplet size for the droplets of the height of the order of a few nanometers is intensively debated. This effect is believed to be related to intermolecular (surface) forces. In the present work, we use the disjoining pressure concept and solve the Derjaguin equation numerically and analytically to model profiles of the sessile droplets of heights comparable with the range of the surface force action. We show that values of the contact angle are dramatically dependent on the droplet height as well as the way the contact angle is defined. For the axisymmetric droplets, the contact angle increases with increasing droplet height, and this dependency becomes universal for different disjoining pressure isotherms when plotted dimensionless with respect to the surface force action range. We demonstrate that for cylindrical droplets, different contact angle definitions can lead to opposite dependencies on the droplet size. We show as well that varying orders of magnitude of the apparent line tension reported can be additionally explained by the contact angle definition chosen.

I. INTRODUCTION

Wetting is omnipresent and occurs when a solid is exposed to a liquid phase. Understanding wetting phenomena is of great significance for a variety of branches of industry, which can be exemplified by nanofluidics [1,2], nanolithography [3], ink-jet printing [4], care products industry [5], food industry [6], and medical products [7]. Despite a long history of wetting science, a manifold of questions still remain unresolved. In particular, understanding the influence of intermolecular forces (usually referred to as surface forces) on statics and dynamic processes is still intensively discussed and requires further investigation [8,9]. Surface forces significantly affect the wetting at nanoscale and, hence, play an important role in nucleation [10,11] and elastocapillarity [12].

In the simplest case one can observe in everyday life, a macroscopic liquid droplet deposited onto a homogeneous flat solid surface either spreads over it or attains an apparent shape of a cap with height and wetted perimeter depending on the properties of the liquid itself, the solid, and the surrounding gas phase. The conventional and, at first glance, simple way for determination of surface wettability is the introduction of a contact angle with which the liquid droplet meets the solid . In most cases, the macroscopic contact angle is defined as a slope of a tangent line in a point of intersection of the liquid-gas interface with the solid surface [13]. The widely employed Young's approach [14] for the contact angle estimation considers a surface energy of each phase and gives the relation

$$\cos\theta_0 = 1 + \frac{S}{\gamma_{LG}}, \tag{1}$$

---

[*] kubochkin@ttd.tu-darmstadt.de

where θ_0 is an equilibrium contact angle and S is the spreading parameter defined as the work required to cover a unit area of a solid with the surface energy γ_{SG} with a liquid by expanding the solid-liquid and liquid-gas interfaces with energies γ_{SL} and γ_{LG}, respectively ($S = \gamma_{SG} - \gamma_{SL} - \gamma_{LG}$). The surface energy of the liquid-gas interface γ_{LG} is denoted γ_0 hereafter for the sake of simplicity. It can be shown within the variational approach that the contact angle set by Eq. (1) is independent of the external fields and of the shape of the droplet [15,16]. However, straightforward application of Young's equation is impossible (even assuming γ_{SG} measurable), since γ_{SL} values cannot be experimentally determined and must be approximated by splitting it into the components. On the other hand, the contact angle within this approach is defined as an angle between the horizontal plane and the tangent line to the liquid-gas interface drawn at the triple line [15,16]. This definition leads to confusion if the sessile drop is surrounded by a thin wetting film.

In many experimental and theoretical studies, it is assumed that the sessile liquid droplet has a shape of a spherical cap if its characteristic size is below the capillary length l_c [17] defined as the length the capillary pressure and the hydrostatic pressure are equal at $l_c = \sqrt{2\gamma/\rho g}$, where the factor 2 corresponds to the axisymmetric droplet, ρ is density of the liquid, and g is the gravitational acceleration. If the drop characteristic length is above l_c, hydrostatic pressure compels the drop to change its shape and to deviate from the spherical cap.

The effects of the droplet size and geometry on the contact angle have been investigated by Vafaei and Podowski [18]. Young-Laplace equations corresponding to long (that is, cylindrical or 2D) and axisymmetric droplets have been solved. It has been reported that the contact angle of 2D droplets does not depend on the droplet volume, whereas for axisymmetric droplets of decreasing volume, the contact angle converges to the asymptotic value, which corresponds to the contact angle of the spherical cap. Yet only capillary forces and gravity effect were considered in their work resulting in the preservation of the contact angle when decreasing the droplet size down to zero.

In the present work, we focus on not that tangible albeit paramount reason why the contact angle does not stay the same for the smaller droplets. We demonstrate a tremendous effect of the surface forces [13,19,20] on the shape and, consequently, on the contact angle of droplets with height comparable to the range of the surface force action. In particular, we show that different trends for the contact angle dependence on the droplet size reported in the literature can be explained by the different ways of the contact angle determination. We report that the dependencies of the contact angle on the dimensionless droplet height collapse to the master curve when the range of the surface force action is chosen as a scaling parameter. We demonstrate that the big differences in the magnitude of the apparent line tension reported by different authors can be caused by the choice of the contact angle definition when the influence of the contact angle hysteresis and surface heterogeneity is absent.

This work is organized as follows. In Sec. II we summarize approaches used to model the wetting at the nanoscale and present a short review of theoretical and experimental works devoted to the statics of nanowetting. The model of the surface forces employed in this work and the governing equations with the boundary conditions are presented in Sec. III. In Sec. IV we focus on the impact of the intermolecular forces on the wetting statics. We evaluate the apparent line tension for different contact angle definitions and, as well, extract the key features of the surface force influence which can gain further understanding of wetting of substrates which can respond to the liquid action by deformations. Finally, we draw conclusions and collect main takeaways.

II. WETTING AT THE NANOSCALE: MAIN APPROACHES AND EXPERIMENTAL EVIDENCES

It is well known that the nanoscale wetting is essentially distinguished from wetting by the macroscopic droplets [13,21–24]. One of the manifestations of such differences owing to the surface force action is the significant variation of the contact angle with the droplet size when the latter is far below the capillary length. This effect has been theoretically as well as experimentally studied for at least last three decades [9,25–29] rendering, nevertheless, controversial results [9,25,29,30]. Three concepts are usually employed when modeling and explaining the experimental findings. Those are

line tension [25,31], Tolman length [21,30], and disjoining pressure [13,22,32,33]. In this section, we discuss each of the concepts alongside the experimental works reporting on the dependence of the contact angle on the droplet size.

A. Line tension and Tolman length

The dependence of the contact angle on the surface forces and on the size of the droplet appears explicitly when using the line tension concept introduced by Gibbs [23]. The line tension is an excess energy the triple contact line possesses itself (the work required to form a unit length of the contact line). Young's equation taking into account the line tension can be written as follows [24,34]:

$$\cos\theta = \cos\theta_0 - \frac{1}{\gamma_0}\left(\frac{\tau}{r_d} + \left|\frac{d\tau}{dr_d}\right|\right)|\cos\phi|, \tag{2}$$

where θ is a microscopic value of the contact angle, τ is the line tension, r_d is the in-plane curvature of the droplet base, and ϕ is the tilt angle of solid formed by the principal normal vector to the contact line and a tangent plane to the substrate surface [33]. The second term in the brackets is referred to as a stiffness coefficient [31] and can be interpreted as a dependency of the apparent line tension on how a surface dividing the liquid and gas phase is defined [34]. Schimmele, Napiórkowski, and Dietrich [31] derived a more general and complex form of equation relating the contact angle with the line tension:

$$\cos\theta = \cos\theta_0 + \frac{1}{\gamma_0 r_d}\left[\left(2\delta\gamma_0 - \left|\frac{d\tau}{d\theta}\right|\right)\sin\theta_0\cos\theta_0 - \tau - r_d\left|\frac{d\tau}{dr_d}\right|\right]. \tag{3}$$

According to them, the contact angle θ may show additional dependence on the stiffness coefficient $\frac{d\tau}{d\theta}|$ and on the Tolman length [21]. The latter reflects the fact that the surface tension of the curved surface is distinguished from that for the plane and depends on the curvature, that is, on the size of the system under consideration. Such a dependency of the surface tension on the size of the system has been obtained by Tolman [21]:

$$\gamma = \frac{\gamma_0}{1 + \frac{2\delta}{R}}, \tag{4}$$

where γ_0 is the surface tension of a planar interface, R is the curvature radius of the droplet surface, and δ is the Tolman length defined as a separation distance between positions of the Gibbs equimolar surface (at which the excess density is zero) and the surface of tension (at which the mechanical definition of tension can be applied [35] and which radius appears in Laplace equation) in a planar interface limit [35,36]. The Tolman length being substituted to (1) also gives us an idea on how θ can alter with respect to the droplet size. However, as is for τ, the sign of δ is also debatable [30].

Despite, according to Amirfazli and Neumann, the stiffness coefficients being important for geometries with high curvatures (nanodroplets) [25], in many cases this is ignored [27–29]. In experimental studies commonly, the well-known form, the so-called "modified Young's equation" [25,27,28],

$$\cos\theta = \cos\theta_0 - \frac{\tau_a}{\gamma_0 r_d} \tag{5}$$

is employed. One should bear in mind, however, that not the pure line tension τ but only apparent line tension τ_a can be obtained via Eq. (5) since the contribution of the components of the apparent line tension is difficult to distinguish [29]. The apparent line tension is, hence, an effective parameter bringing together various effects set by Eq. (3). One can clearly see from (5) that positive values of the apparent line tension cause the contraction of the wetted perimeter and attaining higher values of the contact angle while the negative values oppositely compel it to expand decreasing the equilibrium contact angle.

The line tension concept is actively debated since the measured values of τ_a are reported to be varying in a wide range $\tau_a \sim 10^{-13}$–10^{-4} J/m and also distinguish in sign [9,25,28,29]. The comprehensive reviews of the current state of line tension have been performed by Amirfazli and Neumann [25] and Schimmele, Napiórkowski, and Dietrich [31].

Gaydos and Neumann [37], Duncan *et al.* [38], Amirfazli *et al.* [39], and Amirfazli, Chatain, and Neumann [40] studied the contact angle dependency on the droplet radius using the goniometry technique and obtained the values of the apparent line tension of $\tau_a \sim 10^{-6}$ J/m. Despite droplets with diameters up to 4 mm having been under investigation, the authors found a correlation between the contact angle and the contact radius and, applying the modified Young's equation (5) to the experimental data, obtained τ_a. It is important to note that in those works, hydrophobic surfaces have been used, and the contact angles were found to be decreasing with increasing droplet radius. The axisymmetric droplet shape analysis has been applied for the contact angle determination. Curiously, the experimental results reported by Gaydos and Neumann [37] met good agreement with the theoretical results by Vafaei and Podowski [18] who accounted for only the gravity and capillary pressure in the Young-Laplace equation. Zhao *et al.* [29] examined the nanoscopic droplets on the surfaces possessing different wettability. It has been reported that on the surfaces with low surface energy, the contact angle increases with the increasing contact radius, while on surfaces with the high surface energy the opposite trend is observed. The absolute values of τ_a reported are $\tau_a \sim 10^{-11}$–10^{-10} J/m. The same orders of τ_a have been obtained by Berg, Weber, and Riegler [27] and Heim and Bonaccurso [28]. In their studies enhanced wetting of surfaces by smaller droplets has been reported ($\tau_a < 0$). Zhang *et al.* [41] presented a molecular dynamic simulation of water droplets on surfaces with different wettability. The modeling showed that the contact angles decreased with increasing droplet size for both hydrophilic and hydrophobic surfaces. It has been also shown, however, that the position of the plane dividing solid and liquid phases can play a crucial role in such simulations and can even lead to the change of the sign of the apparent line tension. Atomic force experiments on partial wetting of light alkanes have been conducted by Checco [26]. Values of the apparent line tension agreeing with those Berg, Weber, and Riegler [27], Heim and Bonaccurso [28], and Zhao *et al.* [29] have obtained. However, Checco *et al.* [26] have noted that the surface heterogeneity is likely to affect the dependence of the contact angle on the droplet size. The negative sign of τ_a agrees with that obtained by Heim and Bonaccurso [28]: the smaller droplets have been shown to demonstrate the lower contact angles. In those works, the droplets were assumed to be shaped as parts of spheres, and the contact angles have been defined as the slope at the intersection of the spherical cap fitting and substrate surface. The effect of the curvature of the droplet interface on the contact angle has been discussed and analyzed in terms of the line tension in the work of Das *et al.* [42]. The modeled droplets were assumed to have a shape of the spherical caps, and the contact angles were found to decrease linearly with decreasing radius of curvature of the liquid-gas interface.

It is of interest to notice that the apparent line tension measured by means of using the big droplets [37–40] is of at least five orders higher compared to that for the nanodroplets [27–29], which can be related to the fact that the apparent line tension is not a constant value and also depends on the droplet size. This idea is, on the one hand, in agreement with the experimental results presented by Heim and Bonaccurso [28] and Berg, Weber, and Riegler [27], who reported the nonlinear dependence of $\cos \theta$ on $1/r_d$. However, one should expect smaller values of the line tension for the bigger droplets since the contact angle of the large droplet has to be independent on its size. On the other hand, the fact that the dependence $\cos \theta (1/r_d)$ demonstrates the nonlinear behavior agrees with the findings of Schimmele, Napiórkowski, and Dietrich [31], who stated that values of τ_a in Eq. (5) in fact contain the effects of the stiffness coefficients and the Tolman length additionally to the pure line tension.

According to Eqs. (2) and (3), the Tolman length alongside the stiffness coefficients is believed to affect the apparent line tension. Recently, Kanduč *et al.* [43] combined molecular dynamic simulations of the nanodroplets with their continuum description and showed that the contribution of the stiffness coefficients $\frac{d\tau}{d\theta}|$ can render positive τ_a while τ remains negative. Interestingly, they

also showed the presence of the size effects for the cylindrical droplets albeit less pronounced than for those spherical.

B. Disjoining pressure

The main drawbacks of the line tension and curvature-dependent surface tension concepts are being controversial [9,28,30,44] and the difficulty to distinguish between different contributions: DLVO[1] (van der Waals and electrostatic) and non-DLVO (for example, structural/solvation) forces. Despite the existence of the works on splitting the line tension into components [45–47], it is not commonly used, to the best of the present authors' knowledge.

Another approach eliminating this difficulty and explicitly taking into account interactions not at the triple line but in the thin film and transition zone between the droplet and the film introduces the disjoining pressure $\Pi(h)$, which is an additional pressure arising from the surface layers overlapping.

If only the disjoining pressure is accounted for, the Derjaguin equation for the mechanical equilibrium of the sessile droplet with the adjoining wetting film can be written as

$$\Pi(h) + p_e(r) = \Pi(h_{\mathrm{ads}}), \tag{6}$$

where h_{ads} is a thickness of an equilibrium adsorbed/wetting layer with which a droplet is connected and $p_e = \gamma_0 \varkappa$ is the Laplace pressure equal to the difference between pressure in the gas phase and liquid phase induced by the curvature $\varkappa$. In the case of a liquid wedge or a large droplet ($p_e(0) = 0$), the contact angle can be evaluated using Frumkin-Derjaguin theory [13,19,48] of the disjoining pressure-governed wetting

$$\cos\theta_w = 1 + \frac{1}{\gamma_0} \int_{h_1}^{\infty} \Pi(h)\, dh. \tag{7}$$

The wetting film thickness h_1 can be determined from the equation

$$\Pi(h) = 0. \tag{8}$$

Equation (7), however, cannot be applied for the case of very small droplets, since the curvature-induced Laplace pressure also comes into play altering the interface shape and, consequently, the contact angle. This fact is oftentimes omitted [2]. One of the ways to predict the contact angle behavior has been suggested by Derjaguin, Churaev, and Frumkin, who derived the following equation:

$$\cos\theta = 1 + \frac{p_e(0) h_{\mathrm{ads}}}{\gamma_0} + \frac{1}{\gamma_0} \int_{h_{\mathrm{ads}}}^{\infty} \Pi(h)\, dh, \tag{9}$$

where $p_e(0)$ is the curvature-induced pressure at the droplet apex. It should be noted also that the adsorbed film thickness for the small droplet, in contrast to the liquid wedge, cannot be determined from Eq. (8) because existing pressure $p_e(0)$ affects the thickness of the wetting film. The typical isotherm is shown in Fig. 1 (dark blue curve), and the $p_e(0)$-induced film thickness shift is from h_1 to h_{ads}. One should, however, mind withal that the complete form Frumkin-Derjaguin equation (9) accounting for the curvature-induced pressure has been originally derived for capillaries and droplets assuming that (1) the geometry is 2D (flat capillaries and cylindrical droplets), (2) the liquid-gas interface shape is a part of a circle, and (3) the droplet is not small enough to allow the disjoining pressure to affect its apex [$p_e(0) = \Pi(h_{\mathrm{ads}})$]. The dependency of the contact angle on the droplet size following from Eq. (9) has been pointed out by Boinovich and Emelyanenko [32]: the contact angle increases with the decreasing droplet height.

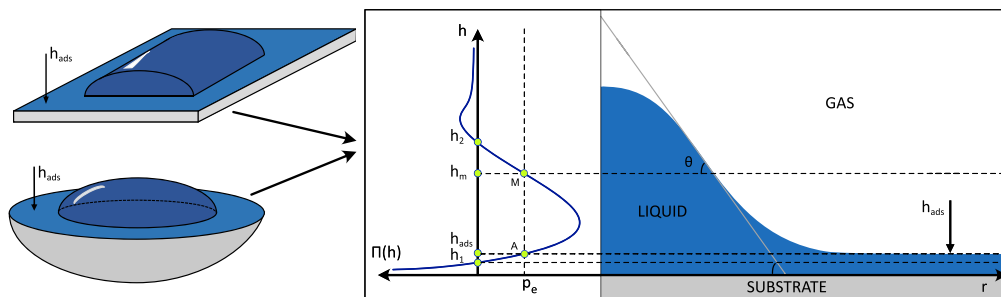[1]A theory of colloidal stability named after Derjaguin, Landau, Verwey, and Overbeek.

FIG. 1. The sessile droplet in equilibrium with its surroundings for the case of pseudopartial wetting. On the left side is the schematic representation of cylindrical and axisymmetric droplets. On the right side, the disjoining pressure as a function of the local droplet height alongside with the droplet profile is shown. The green points are as follows: h_1 is the first root of Eq. (8) corresponding to thickness of the equilibrium adsorbed/wetting layer for the liquid wedge, h_{ads} is the solution of the equation $\Pi(h) + p_e(r) = 0$ corresponding to the thickness of the equilibrium adsorbed layer for the small droplet, h_2 is the second root of Eq. (8) defining the range of the surface force action, and h_m corresponds to the maximal slope (inflection point). In points A and M, the equation $\Pi(h_{ads}) = \Pi(h_m)$ is fulfilled. The contact angle of the droplet is denoted as θ.

The influence of the droplet size on the contact angle has been discussed in the framework of the disjoining pressure theory in several studies. Moldovan *et al.* [49] used scanning polarization force microscopy for investigation of glycerol and sulfuric acid submicrometer droplets on highly oriented pyrolytic graphite and aluminum-covered mica. The authors noted that the surface forces can drastically affect the geometry of the droplets. In particular, an increase of the contact angle with the droplet height was observed for all cases. The same wetting behavior—the contact angle increases and then reaches a plateau—was observed by Xu and Salmeron [50], who studied condensation of glycerol on mica preexposed to air. Xu and Salmeron [50] derived an analytical expression relating the macroscopic contact angle with the nanoscopic contact angle via disjoining pressure. This expression will be discussed in Sec. IV. Influence of the disjoining pressure on the nanodroplets partially wetting the surface was investigated by Samoila and Sirghi [9]. Using the atomic force microscopy, the authors showed that the top of the nanodroplet can be approximated by a spherical cap while the droplet profile departs essentially from the spherical cap shape when approaching the droplet foot. The authors reported that the AFM tip convolution (lower resolution due to the geometry of the tip) had little effect on the shape of the nanodroplets. The nanodroplets attained smaller contact angles, and the approximately threefold difference has been shown between contact angles at the macro- and nanoscale. Experiments employing scanning polarization force microscopy and the continuum mechanic approach involving DLVO surface forces implemented as a disjoining pressure have been suggested by Barberis and Capurro [51] for analysis of the nanodroplet shape. The modeling showed the rising contact angle (defined at the inflection point) with the increasing droplet size as well. However, the parameters of the surface potential in their work were used as the fitting parameters for experimental data, and, hence, no conclusion could have been made regarding their influence as well as regarding the applicability of the spherical cap approximation. Another group of works on a related problem of the liquid-gas interface shape and contact angles in systems with high curvatures consider nanobubbles attached to a solid surface [52]. Those works, however, do not generally discuss the complex and entangled influence of the parameters of the surface forces on the droplet contact angle as well as the wetting film thickness and compare different approaches to the contact angle definition but mostly pursue the particularly chosen systems.

III. MATHEMATICAL FORMULATION OF THE PROBLEM

A. Derjaguin equation and surface force model

Consider a sessile droplet of an incompressible viscous Newtonian liquid deposited onto a flat chemically and physically homogeneous substrate. The substrate is a cylinder of radius r_c, and the droplet is placed in the center of the substrate. The variable h measures the distance between the liquid-gas interface and the substrate the way $h = 0$ corresponds to the substrate surface. Since the pseudopartial wetting case is under investigation in the scope of this work, the substrate is assumed to be covered with an adsorbed/wetting film of an equilibrium thickness h_{ads} (as is shown in Fig. 1). The adsorbed film presence leads to the absence of the distinguishable three-phase contact line, and the contact angle θ in this case can be determined either at the inflection point where the modulus of the first derivative possesses the maximal absolute value that is $\theta = \sup_{r \in [0,r_c]}\{|\tan^{-1}\frac{dh}{dr}|\}$ or at the point of intersection of the spherical (or cylindrical) cap with which the profile is fitted and the substrate plane. The radius of the droplet r_d is defined as the distance between the axis of rotation and the point of intersection of the tangent line built at the inflection point and r-axis. If the spherical cap fitting is used, the r_d is defined as the distance between the axis of rotation and point of intersection of the spherical (or cylindrical) cap and r-axis. The energy of the system can be written as

$$\mathfrak{F} = 2\pi \int \left(\frac{\gamma_0}{2}\left(\frac{dh}{dr}\right)^2 + \mathfrak{S}(h) + \Pi(h_{\text{ads}})h - S \right) r\, dr, \tag{10}$$

where the first term is obtained assuming that $\frac{dh}{dr} \ll 1$, and the term $\mathfrak{S}(h)$ reflects the contribution of the intermolecular forces and is usually referred to as an interfacial potential in literature [2,53]. The interfacial potential can be transformed to the disjoining pressure by a simple relation

$$\mathfrak{S}(h) = \int_h^\infty \Pi(\tilde{h})\, d\tilde{h}. \tag{11}$$

Note that we assume that the dependence of the surface tension on the interface curvature is negligibly small for droplets with small contact angles. We restrict ourselves to effects rendered by the disjoining pressure exclusively. The steady-state profile of the droplet can be obtained by minimization of the energy functional and leads to the equation

$$\frac{d}{dr}\left[\frac{\gamma_0}{r}\frac{d}{dr}\left(r\frac{dh}{dr}\right) + \Pi(h) \right] = 0 \tag{12}$$

with $p_e(r) = \frac{\gamma_0}{r}\frac{d}{dr}(r\frac{dh}{dr})$ which after integration reduces to the Derjaguin equation (6). The boundary conditions for the steady-state Eq. (12) are set as $h = h_d$ at $r = 0$, $\frac{dh}{dr} = 0$ at $r = 0$, and $\frac{dh}{dr} = 0$ at $r = r_c$, where h_d is the maximal height of the droplet. The first boundary condition allows for setting the certain volume of the droplet.

The influence of intermolecular forces is presented in (12) by the disjoining pressure term $\Pi(h)$. According to Derjaguin's theory [13,19] wetting and nonwetting modes are believed to result from different types of the isotherms of disjoining pressure. If only an electrodynamic van der Waals component of disjoining pressure is introduced, the disjoining pressure is written as

$$\Pi(h) = \frac{A}{h^3}, \tag{13}$$

where A is the effective Hamaker constant defined for the three-phase system. Van der Waals interactions can be either repulsive, preventing adsorbed or wetting films from thinning and inherent to the liquids perfectly wetting the solids $\theta_0 = \theta = 0°$, or attractive, which are inherent to the liquid droplets ending up in the nonwetting state.

If the partial wetting case is considered, not only van der Waals but also electrostatic and/or structural forces should be taken into account. For instance, when surfaces in an electrolyte medium

are approaching, the electrostatic double layers (ionic clouds) after reaching the certain critical thickness of the liquid film will overlap inducing an attractive/repulsive force [13,19]. The balance between disjoining and conjoining forces results in the equilibrium contact angle existence when no flow between the droplet and the adjoined liquid film occurs [in that case, the Derjaguin equation or, equivalently, Eq. (12) is fulfilled].

In different works, different models of the disjoining pressure isotherms are used [54–56]. In many cases, the disjoining pressure based on the Lennard-Jones/Mie potential form is adopted [55]. The advantage of such approach is conserving the principal form of the disjoining pressure isotherm containing attractive and repulsive parts and the easier integration and polynomial equations for the equilibrium film thickness. In some works, other functional forms like the sech(h) function are employed to model the attractive term [57].

Throughout this work, we use the electrostatic component in the exponential form obtained within the DLVO theory as a weak overlap approximation for electrostatic force between two planar surfaces and, hence, write the disjoining pressure isotherm as [56,58,59]

$$\Pi(h) = \frac{A}{h^3} - K e^{-\frac{h}{\chi}},$$ (14)

where K is a magnitude of electrostatic forces (referred to as the electric Weber number in Ref. [60]) and χ is the Debye-Hückel screening length [58]. This term can be obtained by using the Yukawa ansatz. The exponential term can describe the effect not only of electrostatic but also of structural forces, albeit not simultaneously [56]. In the latter case, K is a magnitude of the structural forces [19,58] and χ is a characteristic thickness of the hydration layer [22]. That representation agrees with experimental studies [61,62]. Note that in our model, van der Waals interactions alone would lead to the complete wetting and that no oscillating short-range behavior and no electromagnetic retardation are taken into account.

Strictly speaking, all the aforementioned models of the disjoining pressure are applicable only for the films with the uniform thickness, and considering convex or concave surfaces one should take into account that $\Pi = \Pi(h, \frac{dh}{dr}, \frac{d^2h}{dr^2})$ [63]. However, we assume that for the small contact angles the effect of derivative-containing terms of the disjoining pressure can be omitted [9].

B. Scaling, numerical methods, and parameters used

After introduction of the dimensionless variables and parameters in a form

$$\bar{h} = \frac{h}{h_0}, \qquad \bar{r} = \frac{r}{h_0}, \qquad \bar{\chi} = \frac{\chi}{h_0},$$

$$\bar{A} = \frac{A}{\gamma_0 h_0^2}, \qquad \bar{K} = \frac{K h_0}{\gamma_0}, \qquad \bar{\Pi}(\bar{h}) = \frac{\Pi(h) h_0}{\gamma_0},$$

where h_0 is the characteristic length scale to be defined further, Eq. (12) attains the form

$$\frac{d}{d\bar{r}}\left[\frac{1}{\bar{r}}\frac{d}{d\bar{r}}\left(\bar{r}\frac{d\bar{h}}{d\bar{r}}\right) + \bar{\Pi}(\bar{h})\right] = 0.$$ (15)

Note that hereafter all the overbarred variables are considered to be dimensionless.

The MATLAB build-in solver has been employed for solving Eq. (15) and used the collocation method [64]. The mesh for the boundary value problem has been chosen automatically (the tolerance $< 10^{-9}$; further increase of the tolerance did not lead to any significant changes in solution) and has been interpolated to the uniform mesh in order to make the compassion between the solutions available. The variation of the substrate radius r_c led to only negligible differences in the contact angles and was generally less than 0.05%. Additionally, the full Derjaguin equation has been solved. The differences between the solutions were small, and the contact angle's variation did not exceed 0.05%. Therefore, the validity of the gradient-squared approximation has been justified.

TABLE I. Surface force parameters.

Isotherm	A, J	$\bar{A}$	$\bar{K}$	$\bar{\chi}$	$\bar{h}_1$	$\bar{h}_2$	h_2, m	$\theta_w, °$
Case 1A	2.48×10^{-16}	2.689×10^{-5}	0.1624	0.1149	6.66×10^{-2}	1	1.13×10^{-5}	6.98
Case 2A	2.48×10^{-16}	5.189×10^{-5}	0.1792	0.1227	8.28×10^{-2}	1	8.15×10^{-6}	6.98
Case 3A	2.48×10^{-16}	7.372×10^{-5}	0.1904	0.1273	9.3×10^{-2}	1	6.84×10^{-6}	6.98
Case 1B	9.84×10^{-17}	3.982×10^{-5}	0.1717	0.1195	7.59×10^{-2}	1	5.86×10^{-6}	6.98
Case 2B	9.84×10^{-17}	8.838×10^{-5}	0.1972	0.1297	9.86×10^{-2}	1	3.93×10^{-6}	6.98
Case 3B	9.84×10^{-17}	1.445×10^{-4}	0.2188	0.1366	1.15×10^{-1}	1	3.08×10^{-6}	6.98

Equation (15) has a regular singularity at $\bar{r} = 0$. Taking an infinitesimal value of $\bar{r}$ instead of $\bar{r} = 0$, as a direct way to avoid the singularity, did not lead to any change of the solution. The initial guess for the boundary value problem (15) has been chosen in the form of a Gaussian half-bell $\bar{r} \in [0, \bar{r}_c]$: $h_{in} = a e^{-\bar{r}^2/b} + c$, where a, b, and c are constants.

The contact angle for a liquid wedge can be evaluated for this type of the disjoining pressure model using the Frumkin-Derjaguin theory (7)

$$\theta_w = \cos^{-1}\left(1 + \int_{\bar{h}_1}^{\infty} \bar{\Pi}(\bar{h})\, d\bar{h}\right) = \cos^{-1}\left(1 - \bar{K}\bar{\chi}e^{-\frac{\bar{h}_1}{\bar{\chi}}} + \frac{\bar{A}}{2\bar{h}_1^2}\right). \tag{16}$$

Three groups of isotherms have been used for modeling of wetting statics (Table I and Fig. S1 [65]). To show how the surface forces corresponding to different systems can alter wetting behavior of the nanodroplets in those systems while preserving the wetting behavior of the macroscopic droplets, the isotherms have been constructed the way that the contact angle corresponding to the large drop or the liquid wedge (16) remains constant for each isotherm and is equal to $\theta_w = 6.98°$. The dispersion forces are reported to be less sensitive to the changes of the composition of the aqueous solutions [66] than structural and electrostatic forces. Therefore, the Hamaker constants are chosen to be different for two groups, but their dimensional values are preserved within each group. The parameters of electrostatic/structural forces vary within both groups, while the value $\theta_w = 6.98°$ is preserved. Since Eqs. (7) and (16) can be written via the interfacial potential as $\cos\theta_w = 1 + \tilde{\mathcal{S}}(\bar{h}_1)$, the constant contact angle of the wedge θ_w sets the fixed minimum of the interfacial potential [2,53] while allowing for its shape variations.

The heights $\bar{h}_1$ and $\bar{h}_2$ are the roots of Eq. (8) and are as follows:

$$\bar{h}_1 = -3\bar{\chi}\mathcal{W}_0\left(-\frac{\bar{A}^{1/3}}{3\bar{K}^{1/3}\bar{\chi}}\right), \tag{17}$$

$$\bar{h}_2 = -3\bar{\chi}\mathcal{W}_{-1}\left(-\frac{\bar{A}^{1/3}}{3\bar{K}^{1/3}\bar{\chi}}\right), \tag{18}$$

where $\mathcal{W}_i$ is the Lambert $\mathcal{W}$-function with i corresponding to the number of its branch [67]. In the present work we focus on the droplets with heights comparable with the range of the surface force action (Fig. 1). The range of $\bar{h}$ corresponding to the negative pressure conjoining the interfaces is $\bar{h} \in (\bar{h}_1, \bar{h}_2)$. It is natural to take the second root h_2 for the role of the scaling parameter h_0. The dimensionless isotherms are shown in Fig. 2.

The values of the surface force parameters used in this work are distinguished from the typical realistic values inherent to the physical systems. Slightly larger values of the surface force parameters compared to realistic ones have been chosen as has been done in Ajaev *et al.* [56] and Gielok *et al.* [58] in order to reduce the time of calculation and to keep the droplet within the range of the surface force action.
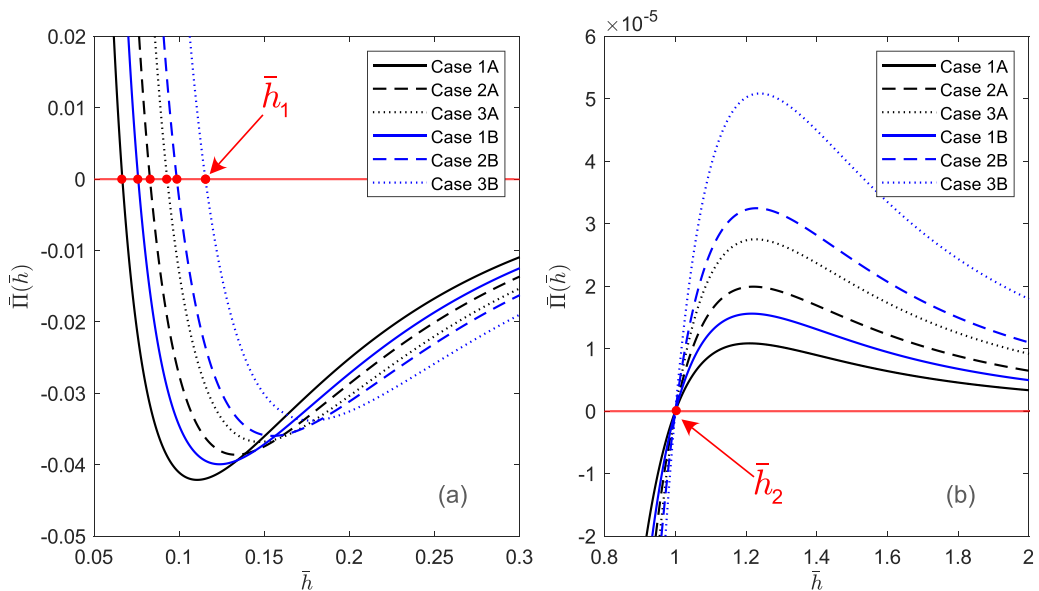
FIG. 2. Disjoining pressure isotherms corresponding to different cases in Table I. Group A is shown in black, group B is shown in blue. (a) The region of the disjoining-conjoining transition. The red markers depict the location of $\bar{h}_1$. The red arrow is to exemplify the location of $\bar{h}_1$ for isotherm 3B. (b) The region of the second conjoining-disjoining pressure transition and the disjoining part of the isotherm responsible for the repulsion between interfaces. The red marker and arrow depict the location of $\bar{h}_2 = 1$.

IV. RESULTS AND DISCUSSION

A. Influence of droplet size on the contact angle: Axisymmetric droplets

In order to obtain the droplet profiles, the steady-state Eq. (15) with the boundary conditions converted to the dimensionless form has been solved. The calculated profiles for the droplet heights $\bar{h}_d$ varying from 0.6 to 6.4 corresponding to case 2B (Table I) are presented in Fig. 3(a). The profiles slightly flatten when $\bar{h}_d$ decreases. Note that the profiles of the similar shape have been experimentally obtained by Giro *et al.* [68].

In the following, we use the profiles presented in Fig. 3(a) to extract the contact angles employing different definitions. In Fig. 3(b) the contact angles of the droplets (we focus first on the contact angles evaluated at the inflection point as we mentioned in Sec. III) are plotted against the droplet heights $\bar{h}_d$ with the teal square markers. As can be seen, the contact angle defined at the inflection point increases as the droplet height increases. It can be also seen that it is smaller than the contact angle θ_w, which the Frumkin-Derjaguin equation (7) for the large droplet gives. The angle θ_w is illustrated by the horizontal solid black line in Fig. 3(b). When the droplet height is equal to the second root of Eq. (8) ($\bar{h}_d = 1$), the contact angle is almost twofold smaller than the Frumkin-Derjaguin angle θ_w. For the bigger droplets, θ approaches the value θ_w that Eq. (7) gives. One of the reasons for these differences is related to the dependence of the adsorbed film thickness $\bar{h}_{\text{ads}}$ on the droplet height $\bar{h}_d$. The adsorbed film thicknesses is illustrated in Fig. 3(b) with the red squares. It increases as the droplet size decreases, and, hence, the smaller droplets are surrounded by thicker wetting films. Additionally, for the smaller droplets, the contribution of the curvature-induced pressure to the shaping of the liquid-gas interface is large since they possess larger curvature at the droplet apex.

According to (9), the contact angle decreases with the increasing droplet height. It results in the dependency opposite to that we obtained solving Eq. (15) and choosing θ at the inflection point $\bar{h}_m$.
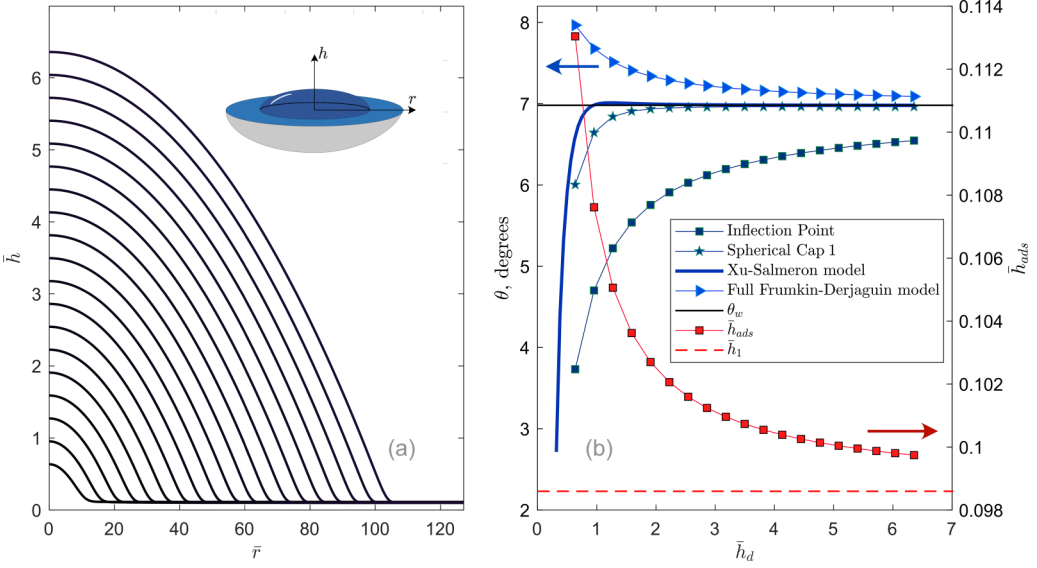
FIG. 3. (a) Stationary droplet profiles obtained from the Derjaguin equation (15) for different heights of droplets $\bar{h}_d$. Isotherm 2B has been used for the profiles depicted. (b) The dependency of the contact angle θ defined at the inflection point on the droplet height $\bar{h}_d$ is shown with teal squares. The contact angles evaluated using the spherical cap of the first kind (see discussion in the text) are marked with teal stars, the contact angle in the Xu-Salmeron model [Eq. (19); see discussion in the text] is shown as a solid blue line. The straight black solid line is to illustrate the contact angle θ_w of the liquid wedge or large droplet [Eq. (7)]. The blue triangles show the contact angles evaluated using the full Frumkin-Derjaguin equation (9). The blue arrow is to show that all teal/blue-marked dependencies belong to the left (angle) axis. The adsorbed/wetting film thickness $\bar{h}_{\text{ads}}$ is shown with red squares. The equilibrium wetting film thickness $\bar{h}_1$ corresponding to the liquid wedge or large droplet is shown with the dashed red line. The red arrow is to show that all red-marked dependencies belong to the right (thickness) axis.

Therefore, the Frumkin-Derjaguin equation in its full form (9) cannot be used for the prediction of the contact angles of axisymmetric droplets. The applicability of Frumkin-Derjaguin equation (9) will be further discussed in Sec. IV C.

Analyzing glycerol droplets wetting mica surfaces, Xu and Salmeron [50] have suggested a theoretical expression for evaluation of the dependence of the contact angle θ on the droplet size $\bar{h}_d$. Integrating the Derjaguin equation (6) using the small slope assumption, the authors obtained the following relation for the contact angle prediction:

$$\theta = \sqrt{\theta_s^2 + 2[\bar{\mathcal{S}}(\bar{h}_d) + \bar{h}_d \bar{\Pi}(\bar{h}_d)]}, \tag{19}$$

where θ_s is the asymptotic value of the contact angle, which can be calculated from the spreading parameter S as $\theta_0^2 = -2S/\gamma$. In order to compare our results with θ obtained from the other definition, θ_0 has been taken equal to θ_w, since both of them describe the static angle of a large drop. Relation (19), however, also differs from the results obtained on the basis of the inflection point [Fig. 3(b), blue solid line]. According to model (19), the contact angle of the wedge θ_w is reached for $\bar{h}_d \approx 1$, whereas the contact angle defined at the inflection point demonstrates much slower growth and asymptotically approaches θ_w at higher $\bar{h}_d$.

Since using a spherical cap approximation is very common in literature as long as $h_d < \sqrt{2\gamma/\rho g}$ [17,27,29,69], the droplet profiles obtained from the numerical experiments have been compared to the spherical caps. Two ways of building the cap over the profile have been used. In the first case, the spherical cap for each profile has been plotted on the basis of three predefined points: the droplet

apex, the inflection point, and the point lying on the grid exactly in the middle between them. We denote the contact angle corresponding to that case θ_2. Another way to determine the spherical cap can be based on the curvature $\bar{\varkappa}(0)$ dictated by the liquid-gas excess pressure at the droplet apex:

$$\bar{p}_e(0) = \bar{\varkappa}(0) = \bar{\Pi}(\bar{h}_{\text{ads}}) - \bar{\Pi}(\bar{h}_d). \tag{20}$$

The contact angle, hence, follows from the simple geometric considerations

$$\theta_3 = \cos^{-1}[1 - \bar{h}_d|\bar{\varkappa}(0)|]. \tag{21}$$

The latter equation, on the other hand, is the simplified version of the modification of the Frumkin-Derjaguin equation accounting for the possible effect of the surface forces at the droplet apex, which has been recently suggested by Iwamatsu [70] for 2D droplets in the form

$$\cos\theta = 1 - \frac{\bar{\mathcal{S}}(\bar{h}_{\text{ads}}) - \bar{\mathcal{S}}(\bar{h}_d) - \bar{\Pi}(\bar{h}_{\text{ads}})\bar{h}_{\text{ads}}}{\bar{\Pi}(\bar{h}_{\text{ads}})}[\bar{\Pi}(\bar{h}_d) - \bar{\Pi}(\bar{h}_{\text{ads}})]. \tag{22}$$

Note, however, that we can apply (21) for both axisymmetric and cylindrical (as has been derived by Iwamatsu [70]) droplets changing the curvature prefactor.

For simplicity, the spherical caps based on the three-point fitting and on Eq. (21) are designated as "Spherical Cap 1" and "Spherical Cap 2" (or "Cylindrical Cap 1" and "Cylindrical Cap 2" for 2D droplets), respectively, in figures below. The contact angle θ_1 defined at the inflection point alongside the contact angles θ_2 and θ_3 following from the assumption on the spherical shape of the droplet (defined at the intersection of the spherical caps with abscissa axis) is presented in Fig. 3(b) and Fig. 4(a). Comparison of the droplet profiles with the spherical cap fittings is shown in Figs. 4(b)–4(d).

The spherical caps of the first kind (three-point-based approach) generally fit the numerically obtained profiles well. At a certain point, the droplet profile relaxes to the wetting film $\bar{h}_{\text{ads}}$, and one can see that it starts to depart from the spherical cap shape and becomes significantly distorted in the transition zone. The departure is more prominent if the droplet height $\bar{h}_d < 1$. The difference in the vicinity of the droplet apex even for the droplets which are fully within the range of the disjoining pressure action can be considered negligible.

Figure 4(a) shows that θ_2 following from the three point-based spherical cap attains higher values compared to θ_1 evaluated at the inflection point. It can be seen indeed that θ_2 for the droplets with $\bar{h}_d \approx 1$ differs from θ_1 by the factor reaching up to ≈ 1.5 [the profiles are shown in Fi. 4(c)]. Increasing $\bar{h}_d$ to a value of 3 [shown in Fig. 4(d)] already allows θ_2 to reach θ_w while θ_1 only slowly approaches θ_w but never reaches it within the set of $\bar{h}_d$ chosen.

The spherical caps based on the curvature that the pressure at the droplet apex dictates also follow the numerically obtained profiles until the triple contact line and are close to the spherical cap based on the three points. However, the spherical caps of the second kind depart from the profile more strongly than those defined by three points. It is especially remarkable for $\bar{h}_d < 1$.

The contact angles obtained within this approximation appear to be slightly higher then θ_2 and, hence, almost twofold larger then θ_1. Similarly, when the droplet height increases, the differences between profiles and contact angles become less pronounced. It is interesting that θ_3 becomes very close θ_w when $\bar{h}_d \approx 1$ as is in the case of the Xu-Salmeron model (19). Indeed, if one looks back, one can see that the contact angle computed from the Xu-Salmeron equation agrees well with the values obtained from the assumption of the spherical cap shape. This can be related to the approximate integration ignoring the details of the droplet profile close to its foot where it relaxes to the wetting film.

Note that the spherical cap approximation legitimacy has been also recently discussed by Giro *et al.* [68]. The deviation of a spherical cap surface from actual droplet topography has been measured by plotting the surface area against the volume for both cases (measured and fitted) and comparing the values. The spherical caps have been reported to underestimate the surface area of droplets as is in our case. However, the authors did not use the contact angles to quantify the wettability and introduced the adsorption energy as a measure of the wettability at nanoscale instead.
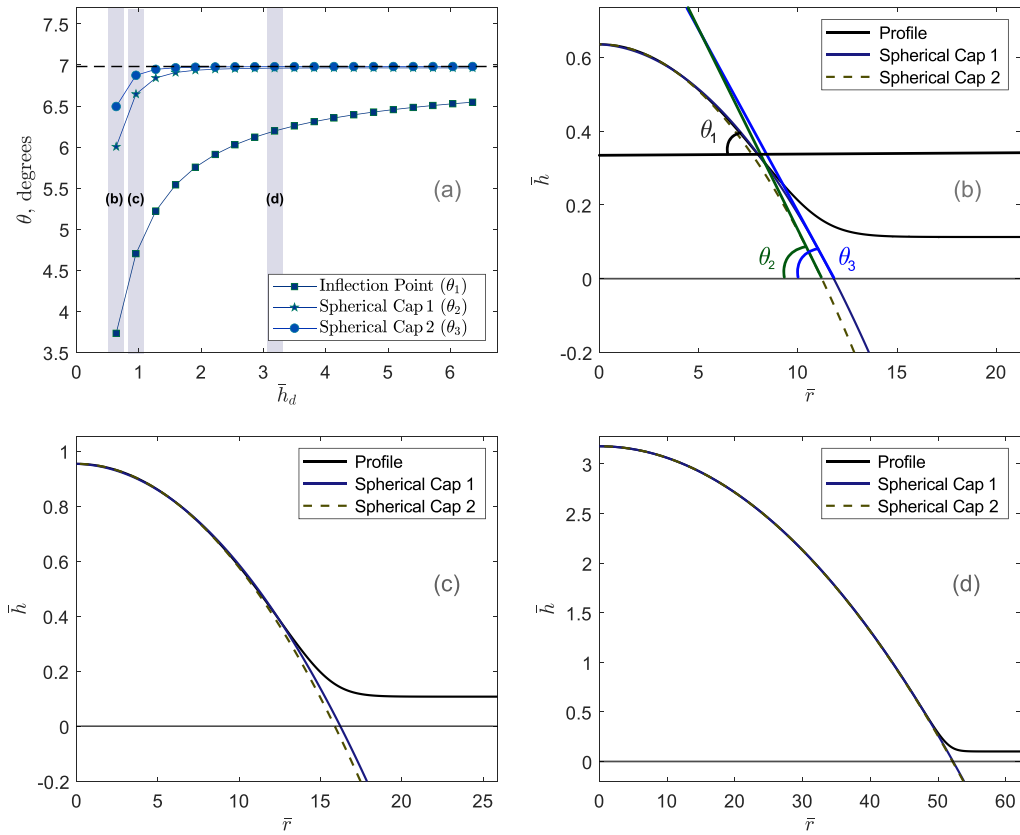
FIG. 4. (a) The dependency of the contact angle θ_1 on the droplet height $\bar{h}_d$ is marked by squares. The contact angles θ_2 and θ_3 estimated using spherical caps of the first and second kinds are marked by stars and circles, respectively. The lines are a guide to the eye. The dashed black line is to illustrate the contact angle θ_w of the liquid wedge or large droplet [Eq. (7)]. Three droplet profiles with different $\bar{h}_d$ have been chosen to show the differences in the profile geometry. Those correspond to panels (b), (c), and (d). The numerically obtained profiles are shown with black solid lines, the spherical caps of the first and second kinds with solid blue and dashed green lines, respectively. (b) The graphical means of the contact angle choice: θ_1 denotes the contact angle defined at the inflection point, θ_2 denotes the angle defined at the intersection of the spherical cap of the first kind with abscissa axis, and θ_3 denotes the angle defined at the intersection of the spherical cap of the second kind with abscissa axis. All profiles correspond to Case 2B.

Consequently, the choice of the contact angle of the nanoscale droplets coexisting with the wetting films is questionable, and treating the droplet as a part of a sphere can result in the significantly different contact angle (compared to the inflection point), especially when the droplet height appears to be within the characteristic range of the disjoining pressure action ($\bar{h}_d < 1$). However, the spherical cap approximation can be justified for relatively big droplets used (the condition $h_d < \sqrt{2\gamma/\rho g}$ is still held), for example, in experiments on wetting and spreading [68,69].

The parameters of the disjoining pressure in the present study differ from those corresponding to real physical systems, and, thus, the question may arise at which scale the size effects reveal themselves. The typical parameters of the disjoining pressure isotherms are $A \sim 10^{-22}$–10^{-21} J, $K \sim 10^5$–10^6 Pa, and $\chi \sim 10^{-8}$–10^{-9} m. The values of the parameters A, K, χ can be found, for example, in the work of Teletzke, Davis, and Scriven [71] or Churaev and Derjaguin [62]. Note, nevertheless, that generally orders of magnitude of K may vary in a wider range depending on the
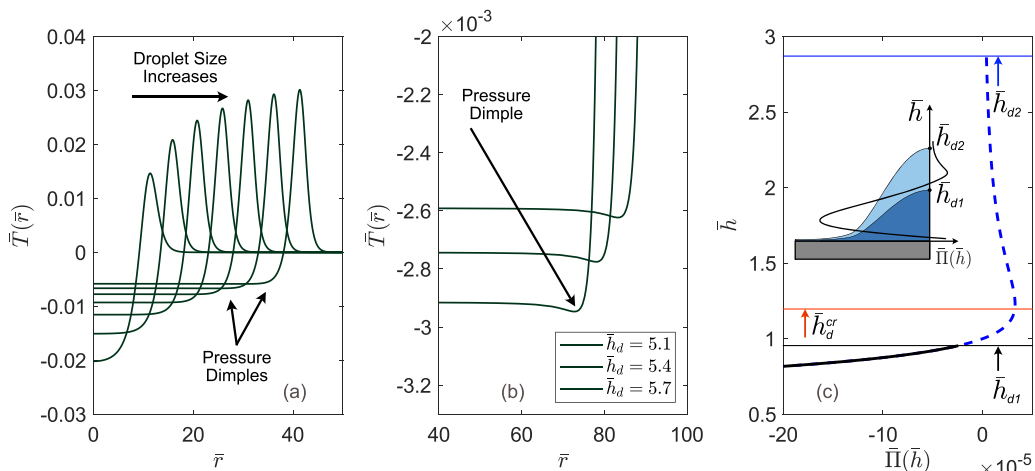
FIG. 5. (a) Traction $\bar{T}(\bar{r})$ (the curvature-induced pressure) distribution over the wetted area. The shape of $\bar{T}(\bar{r})$ under the droplet shows the transition from "sinking" to the dimple emergence occurring as the droplet size increases. The region where the dimples appear is shown by arrows. (b) Pressure dimples emerging for the droplets of $\bar{h}_d > \bar{h}_d^{cr}$. (c) The disjoining pressure distribution along the height of the droplets for which no dimples emerge (solid black line) and dimples emerge (dashed blue line), accordingly. The inset plot is to schematically illustrate the droplet profiles and the disjoining pressure distribution. The plots correspond to the isotherm 2B.

system [61,62]. For the isotherms with the parameters given above, the second root of equation $\Pi(h) = 0$ attains values, which can vary from several nanometers to hundreds of nanometers depending on the system examined. The phenomena examined in the present work are relevant for the dimensionless droplet heights in the range $\bar{h}_d \approx 1–6$. Therefore, we suggest that the effects described afore manifest themselves if the droplet height is in the range up to hundreds of nanometers.

B. Influence of the droplet size on the pressure within the wetted area

Another interesting observation is related to the pressure distribution over the wetted area under the droplet. In the static case, when no flow occurs, the pressure the liquid exerts onto the substrate or so-called traction can be written as [22,72,73]

$$\bar{T}(\bar{r}) = -\bar{\Pi}[\bar{h}(\bar{r})] + \bar{p}_e(0). \tag{23}$$

Combining the first integral of Eq. (15) with $T(\bar{r})$, we obtain

$$\bar{T}(\bar{r}) = \frac{1}{\bar{r}} \frac{d}{d\bar{r}} \left(\bar{r} \frac{d\bar{h}}{d\bar{r}} \right), \tag{24}$$

which is the curvature-induced Laplace pressure. Figure 5(a) shows the Laplace pressure over the wetted area for the cases of different droplet heights $\bar{h}_d$. Both tensile and compressive stresses are exerted onto the substrate [22]. For very small droplets possessing high values of curvature at the apex, the pressure under the droplet is distributed in the way the substrate responses to it by the so-called "sinking" [74]—the droplet causes an ellipsoidal distribution of pressure over the wetted area. Apparently, the sinking cannot be observed for the rigid wetting but becomes prominent when the solid substrate is not rigid anymore (for example, a droplet placed on a layer of a soft gel). Note that the term sinking is also used for describing spreading of droplets over thick liquid layers [75]. If one increases the droplet height, the pressure distribution under the droplet flattens and, at certain $\bar{h}_d$, becomes almost plane-shaped. After that, with further increasing height, the pressure dimple

starts to form [Figs. 5(a) and 5(b)]. We refer to the droplet height at which the dimple forms as a critical droplet height $\bar{h}_d^{cr}$.

The undulation appears away from the contact line region where one could expect such kind of waviness to exist. The explanation of the pressure undulation lays in the S-like shape of the disjoining pressure isotherm [Figs. 1 and 5(c)]. For the droplets with the heights in the range of $\bar{h}_d \in (\bar{h}_1, 1]$, the disjoining pressure isotherm causes only the expected sharp increase of the pressure in vicinity of the contact line. When $\bar{h}_d > 1$, the droplet may be high enough and may contain a level where the isotherm reaches its maximum after crossing the h axis and changing its sign. That imposes an observed peculiarity appearance in the Laplace pressure. We illustrate that by plotting $\bar{\Pi}(\bar{h})$ for two droplets of heights $\bar{h}_{d1} < h_d^{cr}$ and $\bar{h}_{d2} > h_d^{cr}$, accordingly, in Fig. 5(c). Therefore, the value of $\bar{h}_d^{cr}$ can be found directly as the maximum of function $\bar{\Pi}(\bar{h})$ and reads

$$\bar{h}_d^{cr} = -4\chi \mathcal{W}_{-1}\left(-\frac{(3\bar{A})^{1/4}}{4\bar{K}^{1/4}\bar{\chi}^{3/4}}\right). \tag{25}$$

The maximal absolute value of the traction compressing the substrate under the droplet changes with the size of the droplet and can be evaluated as $|\inf_{\bar{r}\in[0,\bar{r_c}]}\{\bar{T}(\bar{r})\}|$ as a function of $\bar{h}_d$. For $\bar{h}_d \leqslant h_d^{cr}$, $|\inf_{\bar{r}\in[0,\bar{r_c}]}\{\bar{T}(\bar{r})\}| = |\bar{\Pi}(\bar{h}_{\text{ads}}) - \bar{\Pi}(\bar{h}(0))|$ while for $\bar{h}_d > h_d^{cr}$ the value of the maximal traction equals $|\inf_{\bar{r}\in[0,\bar{r_c}]}\{\bar{T}(\bar{r})\}| = |-\bar{\Pi}(\bar{h}_d^{cr}) + \Pi(\bar{h}_{\text{ads}})|$ and decreases to the value that the liquid wedge gives:

$$\Big|\inf_{\bar{r}\in[0,\bar{r_c}]}\{\bar{T}(\bar{r})\}\Big| = \big|-\bar{\Pi}\big(\bar{h}_d^{cr}\big)\big|. \tag{26}$$

Therefore, for big droplets, the depth of the dimple is dictated only by the surface force parameters and is not changed with the further size increase.

The distribution of the curvature-induced pressure under the droplet has been shown in a few works [22,33]. However, no analysis on the influence of the droplet size on the depth of the pressure dimple has been presented. The emergence of the dimple leads to the important consequences for the cases when the substrates are not rigid and can respond to the applied pressure by deforming. A discussion of the consequences of our findings for the soft wetting [72,73,76–80] is presented in Sec. S1 of the Supplemental Material [65].

C. Influence of droplet size on the contact angle: Cylindrical droplets

The Derjaguin equation (12) in the case of rotational symmetry and the assumption of the small contact angles can be rewritten as

$$\frac{d^2\bar{h}}{d\bar{r}^2} + \frac{1}{\bar{r}}\frac{d\bar{h}}{d\bar{r}} + \bar{\Pi}(\bar{h}) = \bar{\Pi}(\bar{h}_{\text{ads}}). \tag{27}$$

Unfortunately, Eq. (27) cannot be analytically integrated to extract the explicit dependency $\theta(\bar{h}_d)$ without significant simplification of the disjoining pressure isotherm. It can be suggested, however, that the cylindrical droplet model can be used for the contact angle determination. For example, 2D droplets instead of 3D have been modeled by Iwamatsu [70], Ghosh and Stebe [81], and Heine, Grest, and Webb [82]. In the following, we compare a semianalytical solution of the Derjaguin equation for the cylindrical droplet and numerical solution of Eq. (15) corresponding to the axisymmetric case. Let us highlight that the concept of the disjoining pressure can easily be applied for 2D droplets, whereas it may seem that no size effects are expected to appear within the line tension concept. In fact, one must account not only for a volume, surface, and a line contribution but additionally for the stiffness of the interfaces and contact line [31] when using a variational procedure.
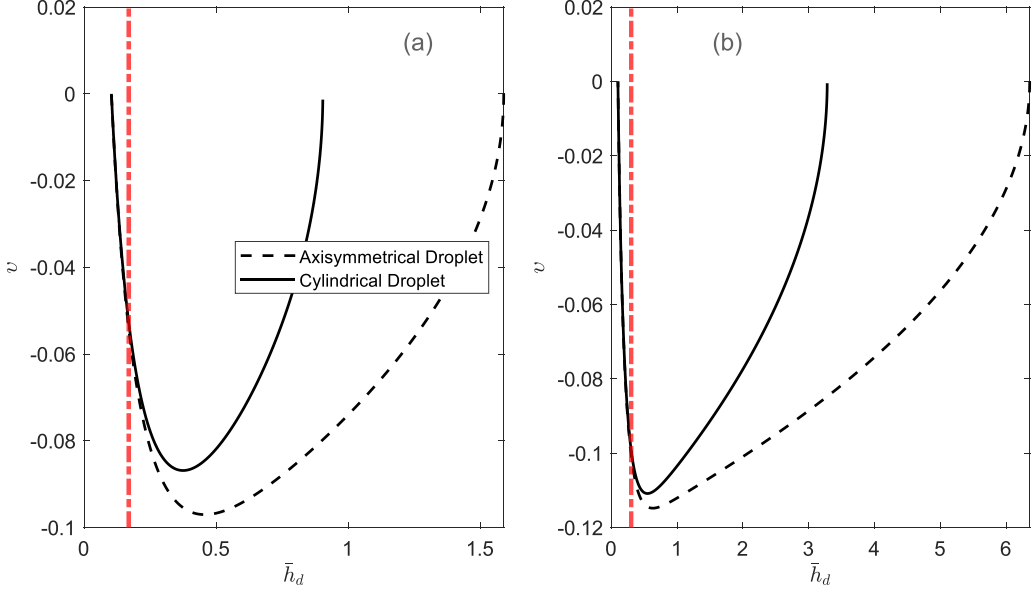
FIG. 6. The slopes v for 2D (cylindrical) droplet obtained from Eq. (28) and 3D (axisymmetric) droplet obtained as a numerical solution of Eq. (15) shown with solid and dashed lines, accordingly, are plotted for $\bar{h}_d = 1.59$ ($\bar{h}_d$ corresponds to 3D droplet) on the left side (a), and for $\bar{h}_d = 6.36$ ($\bar{h}_d$ corresponds to 3D droplet) on the right side (b). The isotherm corresponding to the case 2B is used. The red dash-dotted line is to show the range of $\bar{h}_d$, within which the 2D model demonstrates good agreement with the 3D model.

For the 2D case, the Derjaguin equation within the long-wave approach in dimensionless form (27) can be rewritten as

$$\frac{d^2\bar{h}}{d\bar{x}^2} + \bar{\Pi}(\bar{h}) = \bar{\Pi}(\bar{h}_{\text{ads}}). \tag{28}$$

Introducing variable $v = \frac{d\bar{h}}{d\bar{x}}$, one can write the equation as

$$v^2 = 2\int_{\bar{h}_{\text{ads}}}^{\bar{h}}(\bar{\Pi}(\bar{h}_{\text{ads}}) - \bar{\Pi}(\tilde{h}))d\tilde{h}. \tag{29}$$

Comparison of v evaluated for cylindrical and axisymmetric droplets is presented in Fig. 6. The same $\bar{\Pi}(\bar{h}_{\text{ads}})$ for 2D and 3D droplets has been chosen. The cylindrical droplet model, how it follows from the calculations, is indeed in a good agreement with the axisymmetric model. However, the range of the applicability is very narrow (the height at which major differences between models start to occur is highlighted with a red solid line). The cylindrical droplet has the same values of the slopes for the adsorbed/wetting film region and very close values of the slopes in proximity to the contact line region but distinguished in the inflection point region where v finds its minimum. The range of the applicability increases with increasing droplet height. This is due to the fact that the smaller droplet obtains higher second curvature values quite close to the contact line region. That curvature compels the 3D droplet to distinguish from the 2D case. Therefore, the 2D model cannot be applied for determination of the contact angles in the case of the small droplets with the same $\bar{\Pi}(\bar{h}_{\text{ads}})$ giving lower contact angles but shows better results for bigger drops.

The other way to demonstrate the differences between the cylindrical droplet model and axisymmetric droplet model is to analyze the droplet profiles directly. The analytical solution of Eq. (28)

can be presented in the implicit form

$$\int_{\bar{h}_{\text{ads}}}^{\bar{h}} \frac{d\tilde{h}}{\sqrt{2 \int_{\bar{h}_{\text{ads}}}^{\tilde{h}} [\bar{\Pi}(\bar{h}_{\text{ads}}) - \bar{\Pi}(\hat{h})] \, d\hat{h}}} = \bar{x}_0 - \bar{x}. \tag{30}$$

The form of the disjoining pressure isotherm including the exponential function does not allow for direct integration, and, hence, the integral has been taken numerically. This method is more straightforward for the Lennard-Jones type of the disjoining pressure isotherm.

Following the logic described afore, we analyze the contact angles resulting from profiles (30) and plot dependency of θ on the droplet height $\bar{h}_d$ for three cases when the contact angle is defined (1) in the inflection point (θ_1), (2) at the intersection of the cylindrical cap of the first kind (three-point-based) with abscissa axis (θ_2), and (3) at the intersection of the cylindrical cap of the second kind [Eq. (21)] with the abscissa axis (θ_3). The results are presented in Fig. 7. Note that contact angle θ_2 depends on the location of the points. In the case of 2D profiles the x-grid resulting from the integration (30) is not uniform and the middle point lays closer to the inflection point. The spherical caps, nevertheless, follow the profiles well. Obtaining the solutions in the form $\bar{h}(\bar{x})$ and plotting the spherical caps of the first kind on their basis changes the contact angles only slightly (the variations do not exceed 5%).

As is in the axysimmetric case, the cylindrical caps of both first and second kinds give generally good results on following the profile. However, similarly, the departure from the solution of the Derjaguin equation can be observed close to the contact line for droplets with size $\bar{h}_d < 1$ [Figs. 7(b) and 7(c)], and the cylindrical cap of the first kind follows the profile better than that of the second kind for those small droplets. For cylindrical droplets with $\bar{h}_d > 2$ [Fig. 7(d)] the cylindrical droplet face is almost perfectly circular.

The contact angle (21) for cylindrical nanodroplets has been considered by Iwamatsu [70]. Similarly, a good agreement between the cap and the profile at the droplet top has been reported while in the vicinity of the liquid-solid interface the profiles departed from the cap. The author examined only the cylindrical cap approximation and defined the contact angle at the intersection of the droplet profile with the substrate plane.

The most curious thing, however, appears when quantifying the contact angles that the cylindrical caps of both kinds yield. The contact angles θ_1 defined in the inflection point as well as those θ_2 given by the cylindrical cap of the first kind show an increase with increasing $\bar{h}_d$ as was in the case of axisymmetric droplet, whereas the contact angle θ_3 evaluated with Eq. (21) demonstrates a nonmonotonic dependence on $\bar{h}_d$. θ_3 increases until $\bar{h}_d \approx 1$ and then decreases with increasing droplet height. Note, however, that for $\bar{h}_d < 1$, the cylindrical cap follows the profile approximately until reaching the inflection point $\bar{h}_m$ and then departs. Thus, the values of the contact angles for those $\bar{h}_d$ are questionable. The function $\theta(\bar{h}_d)$ decreasing at $\bar{h}_d > 1$ brings us back to Eq. (9). Plotting $\theta(\bar{h}_d)$ as follows from (9), one can see the perfect agreement between the analytical solution provided by Frumkin, Derjaguin, and Churaev [13] and Starov [22] and results one can obtain using the cylindrical cap assumption (21). The difference between the contact angles evaluated using Eqs. (9) and (21) for $\bar{h}_d < 1$ is apparently related to the assumption made when deriving (9). For the small droplets with height comparable to the surface force action range not only Laplace pressure but also disjoining pressure shapes the droplet apex, which is not accounted for in (9).

Figure 7(a), hence, shows all the insidiousness of the contact angle choice: depending on the definition of the contact angle one can report increasing or decreasing contact angles.

D. Modified Frumkin-Derjaguin equation

Now we derive an equation similar to Eq. (9) for the cylindrical droplets and analytical function $\theta(\bar{h}_d)$ linking the contact angle of the droplet with its height $\bar{h}_d$. However, in contrast to Frumkin, Derjaguin, and Churaev [13], we define the contact angle at the inflection point of the droplet profile ($\theta = \theta_1$) and also, as Iwamatsu [70], account for the disjoining pressure at the droplet apex.
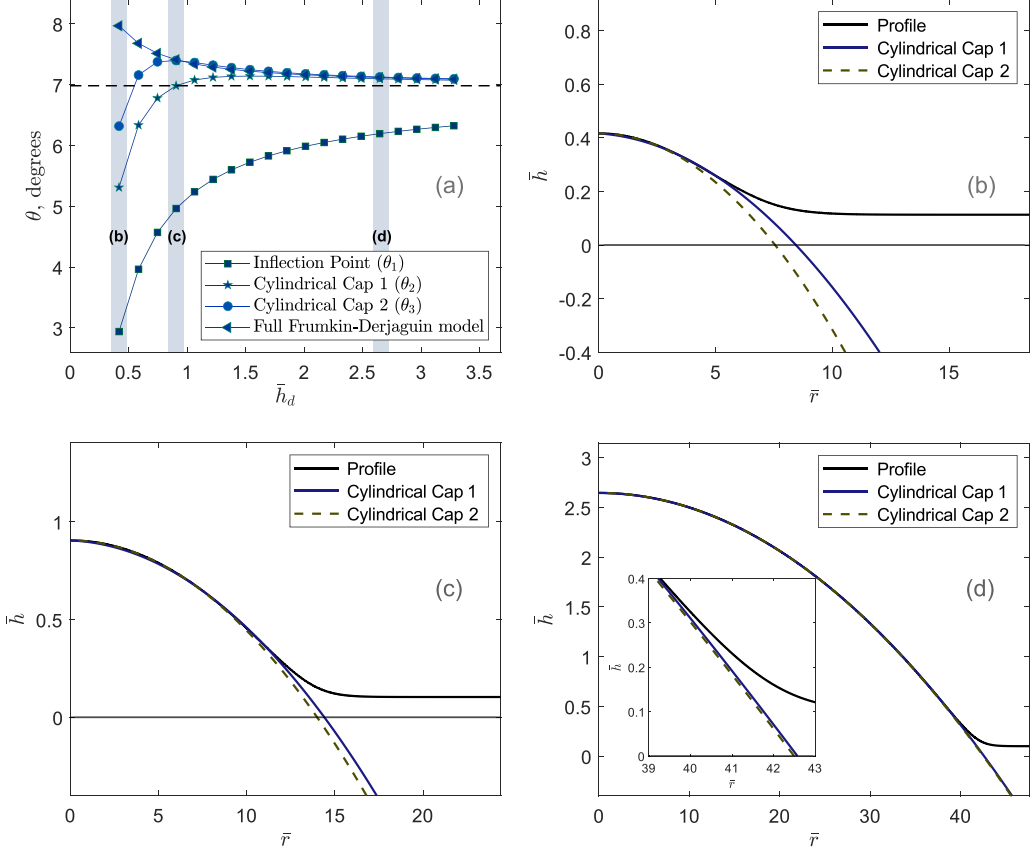
FIG. 7. (a) Contact angles for cylindrical droplets evaluated using different approaches. The dependency of the contact angle θ_1 defined at the inflection point on the droplet height $\bar{h}_d$ is marked with squares. The contact angles evaluated using cylindrical caps of the first and second kinds are marked with stars and circles, respectively. The dashed black line is to illustrate the contact angle θ_w of the liquid wedge or large droplet [Eq. (7)]. The blue triangles show the contact angles evaluated using the full Frumkin-Derjaguin equation (9). The lines are a guide to the eye. Three examples of profiles and cylindrical caps (b), (c), and (d) show the differences in the profiles' geometry. The semianalytically obtained profiles are with black solid lines, and the cylindrical caps of the first and second kinds with solid blue and dashed green lines, respectively. The inset picture in (d) shows the magnified contact line region and departure of the cylindrical caps from the numerically evaluated profile. All profiles were plotted for isotherm 2B.

We start from the first integral of the Derjaguin equation (29). The point at the droplet interface $\bar{h}_m$ corresponding to the maximal slope is the inflection point, which states zero curvature at this point. The latter, in turn, means that the location of this point is determined by the equation

$$\bar{\Pi}(\bar{h}_m) = \bar{\Pi}(\bar{h}_{\text{ads}}). \tag{31}$$

Two solutions of this equation are graphically shown in Fig. 1. Taking into account that $v(\bar{h}_m) = \theta$, one can write the contact angle as

$$\frac{\theta^2}{2} = \int_{\bar{h}_{\text{ads}}}^{\bar{h}_m} [\bar{\Pi}(\bar{h}_{\text{ads}}) - \bar{\Pi}(\bar{h})]d\bar{h} = \bar{\Pi}(\bar{h}_{\text{ads}})(\bar{h}_m - \bar{h}_{\text{ads}}) - \int_{\bar{h}_{\text{ads}}}^{\bar{h}_m} \bar{\Pi}(\bar{h}) \, d\bar{h}. \tag{32}$$

The contact angle of the liquid wedge $\bar{\Pi}(\bar{h}_{\mathrm{ads}})$ is derived as

$$\frac{\theta_w^2}{2} = -\int_{\bar{h}_1}^{\infty} \bar{\Pi}(\tilde{h}) \, d\tilde{h}. \tag{33}$$

Equations (32) and (33) can be transformed to the form similar to the Frumkin-Derjaguin equation for a small droplet (9)

$$\cos \theta = 1 - \bar{\Pi}(\bar{h}_{\mathrm{ads}})(\bar{h}_m - \bar{h}_{\mathrm{ads}}) + \int_{\bar{h}_{\mathrm{ads}}}^{\bar{h}_m} \bar{\Pi}(\bar{h}) \, d\bar{h} \tag{34}$$

and to Eq. (7) for the liquid wedge, accordingly, by applying a small-angle approximation. Combining Eqs. (32) and (33), we arrive at the equation for the contact angle of the cylindrical droplet

$$\frac{\theta^2}{2} = \frac{\theta_w^2}{2} + \bar{\Pi}(\bar{h}_{\mathrm{ads}})(\bar{h}_m - \bar{h}_{\mathrm{ads}}) + \int_{\bar{h}_m}^{\bar{h}_{\mathrm{ads}}} \bar{\Pi}(\bar{h}) \, d\bar{h} + \int_{\bar{h}_1}^{\infty} \bar{\Pi}(\bar{h}) \, d\bar{h}. \tag{35}$$

A relation between $\bar{h}_d$ and $\bar{h}_{\mathrm{ads}}$ can be built from the condition at the droplet apex where $v = 0$, and, hence, it reads

$$\bar{\Pi}(\bar{h}_{\mathrm{ads}})(\bar{h}_d - \bar{h}_{\mathrm{ads}}) - \int_{\bar{h}_{\mathrm{ads}}}^{\bar{h}_d} \bar{\Pi}(\bar{h}) \, d\bar{h} = 0 \tag{36}$$

or equivalently from the Derjaguin equation

$$\bar{\Pi}(\bar{h}_d) = \bar{\Pi}(\bar{h}_{\mathrm{ads}}) - \bar{p}_e(0), \tag{37}$$

which is easier and more convenient, but cannot be applied directly in those cases when the droplet is small but nevertheless under the negligible action of the surface forces in its apex. Therefore, in the most general case function $\theta(\bar{h}_d)$ can be written as

$$\frac{\theta^2(\bar{h}_d)}{2} = \frac{\theta_w^2}{2} + \frac{\int_{\bar{h}_{\mathrm{ads}}}^{\bar{h}_d} \bar{\Pi}(\bar{h}) \, d\bar{h}}{\bar{h}_d - \bar{h}_{\mathrm{ads}}} (\bar{h}_m - \bar{h}_{\mathrm{ads}}) + \int_{\bar{h}_m}^{\bar{h}_{\mathrm{ads}}} \bar{\Pi}(\bar{h}) \, d\bar{h} + \int_{\bar{h}_1}^{\infty} \bar{\Pi}(\bar{h}) \, d\bar{h} \tag{38}$$

or using the interfacial potential form

$$\frac{\theta^2(\bar{h}_d)}{2} = \frac{\theta_w^2}{2} + \frac{\bar{\mathfrak{S}}(h_{\mathrm{ads}}) - \bar{\mathfrak{S}}(\bar{h}_d)}{\bar{h}_d - \bar{h}_{\mathrm{ads}}} (\bar{h}_m - \bar{h}_{\mathrm{ads}}) + \bar{\mathfrak{S}}(\bar{h}_m) + \bar{\mathfrak{S}}(\bar{h}_1) - \bar{\mathfrak{S}}(\bar{h}_{\mathrm{ads}}). \tag{39}$$

Thus, both dependencies $\theta(\bar{h}_d)$—increasing and decreasing depending on the definition of the contact angle—can be obtained analytically. It is of necessity to notice, however, that in the case of the liquid wedge or the large droplet, θ_w is defined as the constant value v reaches at $h \to \infty$. Therefore, the maximum angle θ_f reached with the increasing droplet size is not θ_w but is defined by

$$\frac{\theta_f^2}{2} = \lim_{\bar{h}_d \to \infty} \frac{\theta^2(\bar{h}_d)}{2} = \bar{\mathfrak{S}}(1) - \bar{\mathfrak{S}}(\bar{h}_1), \tag{40}$$

which can be written in the dimensional form accounting for Eq. (7) as

$$\cos \theta_f = \cos \theta_w - \frac{\mathfrak{S}(h_2)}{\gamma}. \tag{41}$$

E. Effect of the electrostatic/structural interactions on the equilibrium microscopic contact angle

In this subsection, we show how parameters responsible for electrostatic and structural interactions can affect the interface shape of the smaller droplet while preserving θ_w. Note that constant θ_w fixes the minimum of the interfacial potential while allowing for the variations of its shape.
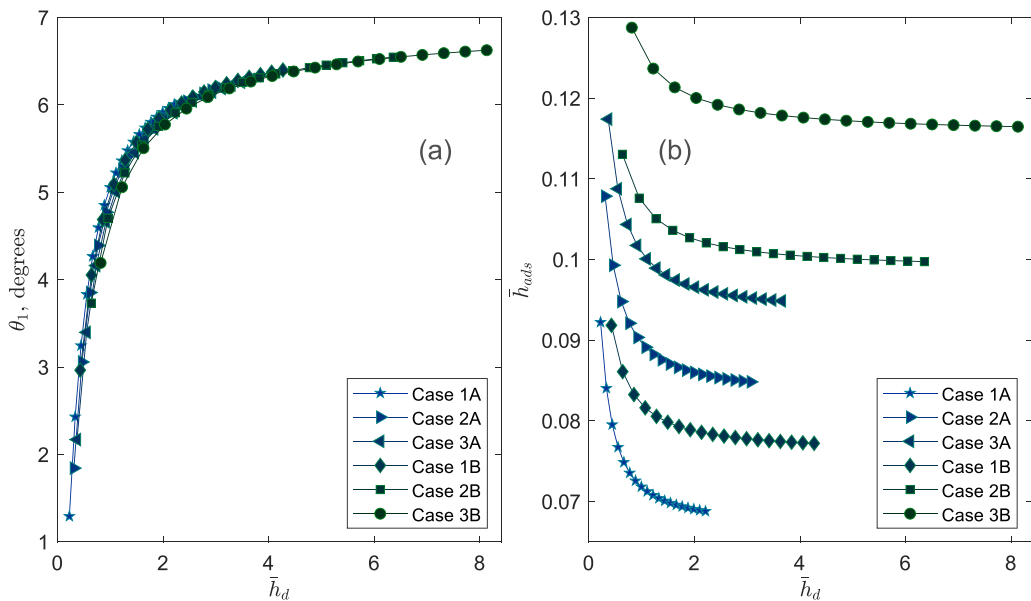
FIG. 8. (a) Influence of the surface forces on the dependence of the contact angle on the dimensionless droplet height for the axisymmetric droplet. The contact angle is defined at the inflection point. (b) Dependence the dimensionless adsorbed/wetting film thicknesses on the dimensionless droplet height.

The dependence of θ (defined at the inflection point, $\theta = \theta_1$) on $\bar{h}_d$ for different disjoining pressure isotherms (Table I) is presented in Fig. 8(a). The curves $\theta(\bar{h}_d)$ plotted for all isotherm collapse and generally can be considered as a "master curve" and used for the contact angle prediction based on the ratio of the droplet height and the second root of Eq. (8): $\bar{h}_d = h_d/h_2$.

The thicknesses of the adsorbed/wetting films $\bar{h}_{\text{ads}}$ corresponding to the different droplet heights $\bar{h}_d$ are presented in Fig. 8(b). One can see that the smaller droplets have the thicker adjoining wetting films. However, despite the fact that the dependence $\bar{h}_{\text{ads}}(\bar{h}_d)$ is similar for all isotherms, the curves do not collapse to one master curve. The dependency of the contact angle on the dimensional droplet height for different disjoining pressure isotherms alongside a discussion of the influence of the dimensional parameters of the isotherms on it can be found in Sec. S2 of the Supplemental Material [65].

The similar master curve $\theta(\bar{h}_d)$ can be observed in the case of cylindrical droplets [Fig. 9(a)]. In order to explain this behavior, we restrict ourselves to analyzing very small droplets with the height $\bar{h}_d < 1$. We further use a simplified disjoining pressure isotherm depicted in Fig. 9(b). We assume that in this simplified form, the branch of the isotherm $d\bar{\Pi}/d\bar{h} > 0$ has a constant slope. The branch of the isotherm $d\bar{\Pi}/d\bar{h} < 0$ has also a constant slope, which is steep that it can be assumed that $\bar{h}_{\text{min}} - \bar{h}_1 \ll 1$ where $\bar{h}_{\text{min}}$ is the height corresponding to the minimum of the disjoining pressure isotherm $\bar{\Pi}_{\text{min}}$.

Using Eq. (32) and simple geometry of the isotherm [Fig. 9(b)], one can write the slope of the droplet at any height $\bar{h}$ as

$$\frac{v^2}{2} = \bar{\Pi}(\bar{h}_{\text{ads}})(\bar{h} - \bar{h}_1) - \frac{\bar{\Pi}_{\text{min}}(2 - \bar{h} - \bar{h}_1)(\bar{h} - \bar{h}_1)}{2(\bar{h} - \bar{h}_1)}. \tag{42}$$
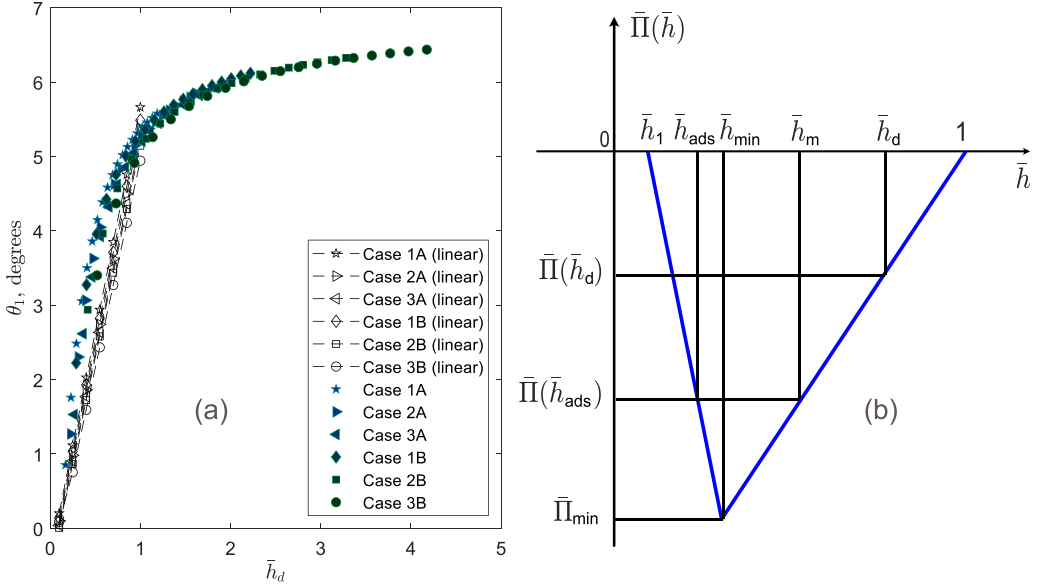
FIG. 9. (a) Dependencies of the contact angle on the dimensionless height of the cylindrical (2D) droplet obtained with Eq. (44) (shown with empty black markers connected with dashed lines) as well as the contact angles resulting from the solution of the Derjaguin equation (28) (shown with filled colored markers). (b) The simplified disjoining pressure isotherm (solid blue line) where $\bar{h}_1$ is the dimensionless thickness of the equilibrium adsorbed/wetting film for the liquid wedge, $\bar{h}_{ads}$ is the dimensionless thickness of the adsorbed/wetting film for the droplet, $\bar{h}_{min}$ is the height at which the disjoining pressure attains its minimal value $\bar{\Pi}_{min}$, $\bar{h}_m$ corresponds to the inflection point, and $\bar{h}_2 = 1$ defines the range of the surface force action.

After that, Eq. (36) can be employed in order to relate the height of the inflection point $\bar{h}_m$ with the height of the droplet $\bar{h}_d$. That results in a simple equation

$$\bar{h}_m = \frac{\bar{h}_1 + \bar{h}_d}{2}, \tag{43}$$

which together with Eqs. (32) and (42) results, in turn, in the equation for the contact angle of the cylindrical droplet as a function of its height

$$\theta = \frac{\bar{h}_d - \bar{h}_1}{2} \sqrt{\frac{\bar{\Pi}_{min}}{(\bar{h}_1 - 1)}}. \tag{44}$$

The latter can be rewritten using Eq. (40) defining the contact angle θ_f, which larger droplets eventually reach:

$$\theta = \frac{\bar{h}_d - \bar{h}_1}{1 - \bar{h}_1} \theta_f. \tag{45}$$

The contact angles obtained with Eq. (44) as well as the contact angles resulting from the solution of the Derjaguin equation (28) are presented in Fig. 9(b). As one can see, the agreement is very good, and a similar master curve results from the simplified consideration.

Despite the fact that the dependence of the contact angle on the scaled droplet height $\bar{h}_d$ does not show universality in its strict definition (θ still depends on $\bar{h}_1$), we suggest that the variation of the shapes of interfacial potential does not lead to significant departure of $\theta(\bar{h}_d)$ from each other, when the minimum of the interfacial potential is fixed.
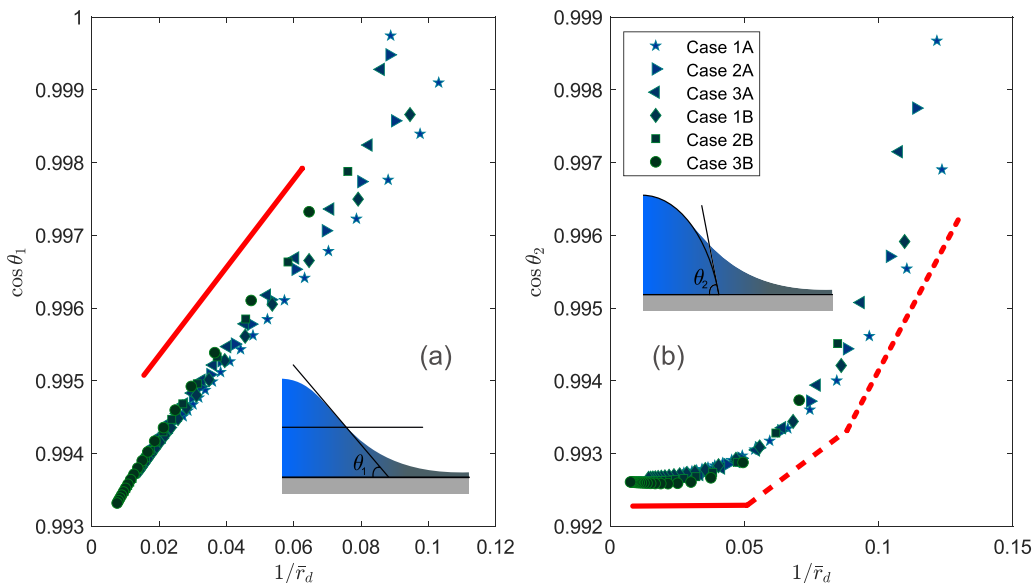
FIG. 10. The dependency of the contact angle θ on the dimensionless curvature of the three-phase contact line $1/\bar{r}_d$ (a) for the contact angle defined at the inflection point and (b) for the contact angle defined at the intersection of the spherical cap of the first kind (three-point-based) with abscissa axis. Inset schematic pictures illustrate the way that the contact angle is defined. The solid red lines are a guide for the eye and schematically show the slopes required for the apparent line tension evaluation.

F. Apparent line tension of axisymmetric droplets

Despite the fact that the line tension concept is generally a macroscopic concept, it is often applied for the nanodroplets. The modified Young's equation (5) is commonly used for determination of the line tension [27–29,41]. In fact, as has been demonstrated by Schimmele, Napiórkowski, and Dietrich [31], only the apparent line tension τ_a can be obtained this way [29,41]. In the following, we show that for the nanoscopic droplet profiles, one may obtain different values of τ_a depending on the definition of the contact angle chosen.

In Figs. 10(a) and 10(b) cosines of the contact angles plotted against curvature of the triple line are shown for two definitions of the contact angle. In Fig. 10(a) the contact angles θ_1 defined at the inflection point are shown and in Fig. 10(b) the spherical cap of the first kind has been used to obtain the contact angles θ_2. Note that using the contact angle defined via Eq. (21) (spherical cap of the second kind) results in a dependency very close to that depicted in Fig. 10(b), and, hence, we do not present it. As has been stated in Sec. III, when the contact angle is defined at the inflection point, we define $\bar{r}_d$ as the distance between the axis of rotation and the point of intersection of the tangent line built at the inflection point and $\bar{r}$-axis. For the spherical cap of the first kind, $\bar{r}_d$ is defined as the distance between the axis of rotation and the point of intersection of the spherical (or cylindrical) cap and $\bar{r}$-axis.

The dependencies $\cos\theta(1/r_d)$ are conventionally employed for the evaluation of the apparent line tension τ_a [27,28,39,40]. In many works [29,39], functions $\cos\theta(1/r_d)$ were found linear, while in another group of experimental works [27,28] a necessity to account for additional terms or second order in the modified Young's equation (5) was reported. Interestingly, we also observe different shapes of $\cos\theta(1/\bar{r}_d)$ curves for different contact angle definitions, and, what is also of importance, the curves in both cases collapse to one master curve.

Let us average the data for the collapsing curves $\cos\theta(1/\bar{r}_d)$ depicted in Fig. 10(a) and evaluate the dimensionless apparent line tension $\bar{\tau}_a = \frac{\tau_a}{\gamma_0 h_2}$ using Eq. (5). When the contact angle is

defined at the inflection point (where the profile can be considered following the spherical cap), the curve perfectly fits with the linear trend giving $\bar{\tau}_a \approx -6.6 \times 10^{-2}$. If the surface tension is $\gamma_0 \approx 72 \times 10^{-3}$ J/m^2, that results in $|\tau_a| \sim 10^{-3} \times h_2$. In our case ($h_2 \sim 10^{-6}$–$10^{-5}$ m, Table I), $|\tau_a| \sim 10^{-9}$–10^{-8} J/m, while for $h_2 \sim 10^{-9}$–10^{-7} m (corresponding to the real isotherm parameters), we have $|\tau_a| \sim 10^{-12}$–10^{-10} J/m. The latter values agree with the those obtained by Berg, Weber, and Riegler [27], Heim and Bonaccurso [28], Zhao *et al.* [29], and Zhang *et al.* [41].

According to Fig, 10(b), the situation is more complex. When the spherical cap of the first kind is used to obtain the contact angle, the dependence of the contact angle θ_2 on the dimensionless curvature of the three-phase contact line $1/\bar{r}_d$ is not linear. The apparent line tension is still negative but is not a constant anymore being dependent on the droplet size. The function is fitted better with polynomials. Remarkably, $\bar{\tau}_a \to 0$ when $\bar{h}_d \to \infty$, which is physically convincing because the contact angle of the large droplet is not to change with the size. However, that faces the contradiction with the results presented by Heim and Bonaccurso [28] who reported higher values of the apparent line tension for bigger droplets.

Yet we highlight once again that only the apparent line tension can be captured by the modified Young's equation in form (5). Therefore, the values τ_a still contain the stiffness coefficients and the Tolman length term, and no conclusion can be drawn about the sign and the magnitude of the pure line tension, τ.

V. CONCLUSIONS

In this work, employing the disjoining pressure concept, we investigated the influence of the droplet size and surface forces on the contact angle of sessile droplets of height comparable with the range of the surface forces action. The Derjaguin equation in the case of low contact angles has been used for obtaining the steady-state profiles of the droplets.

We have shown that the equilibrium contact angle is generally dramatically dependent on the droplet size. That results from the interplay of the surface forces and curvature-induced pressure, which is often omitted. In the case of the axisymmetric droplets, the contact angle increases with increasing droplet height. It differs from the contact angle predicted by the Frumkin-Derjaguin theory and reaches it only when the droplet is large (but is still below the capillary length). We demonstrated that the contact angle at nanoscale is highly sensitive to the way it is defined—via the spherical cap approximation or at the inflection point—which impacts the values of the contact angle and can lead to those distinguishing from each other by almost 100%.

The contact angles of cylindrical (2D) droplets show noticeable difference compared to those of the axisymmetric droplets and are in agreement with them only for the cases of the relatively big droplets (which are still below the capillary length). It has been shown that different ways of the contact angle definition can lead not only to the different values but also to the opposite trends when considering the size effects.

The electrostatic/structural forces are shown to affect the contact angle of the sessile droplet. However, the dependencies of the contact angle on the droplet height for the disjoining pressure isotherms keeping the contact angle of the wedge (the interfacial potentials have the same minimum) collapse to the master curve when plotted dimensionless with respect to the range of the surface force action. This finding can be used for prediction of the contact angle for different nanosystems having, nevertheless, the same contact angle for the large droplet. We developed the simple model in order to show the reasons behind this behavior.

In the present work, we have additionally summarized the dependencies of the contact angle on the droplet height obtained analytically in previous work [13,50,70] and have derived the equation for the evaluation of the contact angle defined at the inflection point for the cylindrical droplets. Therefore, all trends of contact angle alterations with the droplet height—decreasing, nonmonotonic, and increasing—can be mathematically described.

The applicability of the commonly used spherical and cylindrical cap approximation has been discussed for both axisymmetric and cylindrical droplets. Despite the common belief in its

applicability for droplets with height smaller than capillary length [17,47], it has been concluded that the profiles of droplets with height comparable to the range of the surface force action strongly deviate from the spherical (cylindrical) cap shape. The significant distortion of the droplet shape is caused by the surface forces.

We suggest, nevertheless, that there is no preferable way for the contact angle definition applicable for all cases. Defining the contact angle at the inflection point may seem a very good strategy since it introduces no ambiguity in contrast to the other definitions. This way of contact angle determination can be easily adopted in theoretical/numerical studies. However, it does not have a counterpart at macroscopic level, and, hence, a perfectly defined (down to the nanometric foot of the droplet) profile is required for the evaluation of the contact angle. In experimental studies of nanodroplets, the position of the inflection point is usually unavailable due to technical reasons. In rare cases, when the position of the inflection point can be detected, great care has to be taken for the elimination of the tip convolution effects (for example, if the AFM technique is used). All that complicates the application of the inflection point definition for the experimental studies. Therefore, the spherical (cylindrical) cap approximation (or its variations) remains the easiest way to characterize the wettability since it can be applied even in the cases of the scattered data. However, the procedure of the fitting of the droplet profile must be clearly stated to avoid any confusion.

The contact angle dependence on the three-phase contact line curvature is conventionally used for the evaluation of the apparent line tension [28,29,39,41]. To the best of the authors' knowledge, for the first time, it has been pointed out that the way the contact angle defined significantly affects the magnitude of the apparent line tension value. Therefore, the wide range of the line tension values reported in the literature [9,25] can be related to the contact angle definition. Other reasons of the wide range of the line tension values reported are scattering in the experimental results [41], peculiar behavior of some of the liquid systems under consideration, and contact angle hysteresis. The dimensionless apparent line tension for all contact angle definitions presented can be considered to be dependent only on the second root of the disjoining pressure isotherm when the surface tension of the liquid is set constant. Similarly to the contact angle, it can be predicted for different isotherms as long as the contact angle of a large droplet (minimum of the interfacial potential) is kept preserved.

It has been found that above the critical droplet height curvature-induced Laplace pressure shows nonmonotonic behavior within the wetted area: the pressure undulation related to the S-shaped disjoining pressure isotherm can be observed. These findings are in agreement with the experimental results reported [78] and can find applications when considering soft surfaces.

Future work could aim to reveal the contact angle dependence on the droplet size for droplets on hydrophobic surfaces since in that case low contact angle approximation cannot be applied and, in addition, the disjoining pressure must contain curvature-dependent terms [83]. Also, the size-dependent line tension that appeared in recent studies and showed larger values for larger droplets [27,28] is in contradiction with the theory and requires further investigation. The present work could be also extended by considering spreading processes over rigid and soft surfaces for the droplets comparable with the surface force action range since the number of works on such systems is still limited.

[1] T. Pfohl, F. Mugele, R. Seemann, and S. Herminghaus, Trends in microfluidics with complex fluids, ChemPhysChem **4**, 1291 (2003).

[2] M. Rauscher and S. Dietrich, Wetting phenomena in nanofluidics, Annu. Rev. Mater. Res. **38**, 143 (2008).

[3] Y. Deng, Z. Liu, Y. Wang, H. Duan, and J. G. Korvink, Micro-textures inversely designed with overlayed-lithography manufacturability for wetting behavior in Cassie–Baxter status, Appl. Math. Model. **74**, 621 (2019).

[4] B. He, S. Yang, Z. Qin, B. Wen, and C. Zhang, The roles of wettability and surface tension in droplet formation during inkjet printing, Sci. Rep. **7**, 11841 (2017).

[5] A. Trybala, A. Bureiko, N. Kovalchuk, O. Arjmandi-Tash, Z. Liu, and V. Starov, Wetting properties of cosmetic polymeric solutions on hair tresses, Colloids Interface Sci. Commun. **9**, 12 (2015).

[6] L. Lapčík, B. Lapčíková, H. Žižková, P. Li, and V. Vojtekova, Effect of cocoa fat content on wetting and surface energy of chocolate, Potravinarstvo Slovak J. Food Sci. **11**, 410 (2017).

[7] J. Choi, W. Kim, and H.-Y. Kim, Crack density in bloodstains, Soft Matter **16**, 5571 (2020).

[8] V. M. Starov and M. G. Velarde, Main problems in kinetics of wetting and spreading to be solved, in *Wetting and Spreading Dynamics* (CRC Press Taylor & Francis Group, Boca Raton, 2020), pp. 465–465.

[9] F. Samoila and L. Sirghi, Disjoining pressure in partial wetting on the nanoscale, Langmuir **33**, 5188 (2017).

[10] F. Kuni, A. Shchekin, A. Rusanov, and B. Widom, Role of surface forces in heterogeneous nucleation on wettable nuclei, Adv. Colloid Interface Sci. **65**, 71 (1996).

[11] S. K. Singha, P. K. Das, and B. Maiti, Inclusion of line tension effect in classical nucleation theory for heterogeneous nucleation: A rigorous thermodynamic formulation and some unique conclusions, J. Chem. Phys. **142**, 104706 (2015).

[12] J. Bico, É. Reyssat, and B. Roman, Elastocapillarity: When surface tension deforms elastic solids, Annu. Rev. Fluid Mech. **50**, 629 (2018).

[13] B. V. Derjaguin, N. V. Churaev, and V. M. Muller, *Surface Forces* (Springer, New York, 1987).

[14] J. W. Drelich, L. Boinovich, E. Chibowski, C. D. Volpe, L. Hołysz, A. Marmur, and S. Siboni, Contact angles: History of over 200 years of open questions, Surface Innovations **8**, 3 (2020).

[15] E. Bormashenko, Young, Boruvka–Neumann, Wenzel and Cassie–Baxter equations as the transversality conditions for the variational problem of wetting, Colloids Surf. A **345**, 163 (2009).

[16] E. Bormashenko, Physics of solid–liquid interfaces: From the Young equation to the superhydrophobicity (review article), Low Temp. Phys. **42**, 622 (2016).

[17] Y. Wu, F. Wang, S. Ma, M. Selzer, and B. Nestler, How do chemical patterns affect equilibrium droplet shapes? Soft Matter **16**, 6115 (2020).

[18] S. Vafaei and M. Podowski, Analysis of the relationship between liquid droplet size and contact angle, Adv. Colloid Interface Sci. **113**, 133 (2005).

[19] V. M. Starov and M. G. Velarde, Surface forces and wetting phenomena, J. Phys.: Condens. Matter **21**, 464121 (2009).

[20] Q. Xie, Y. Chen, L. You, M. Hossain, and A. Saeedi, Drivers of wettability alteration for oil/brine/kaolinite system: Implications for hydraulic fracturing fluids uptake in shale rocks, Energies **11**, 1666 (2018).

[21] R. C. Tolman, The effect of droplet size on surface tension, J. Chem. Phys. **17**, 333 (1949).

[22] V. M. Starov, M. G. Velarde, and C. J. Radke, *Wetting and Spreading Dynamics* (CRC Press, Boca Raton, FL, 2007).

[23] J. W. Gibbs, *Scientific Papers Vol, 1: Thermodynamics* (Longman, New York, 1906).

[24] A. I. Rusanov, Problems of surface thermodynamics, Pure Appl. Chem. **64**, 111 (1992).

[25] A. Amirfazli and A. Neumann, Status of the three-phase line tension: A review, Adv. Colloid Interface Sci. **110**, 121 (2004).

[26] A. Checco, H. Schollmeyer, J. Daillant, P. Guenoun, and R. Boukherroub, Nanoscale wettability of self-assembled monolayers investigated by noncontact atomic force microscopy, Langmuir **22**, 116 (2006).

[27] J. K. Berg, C. M. Weber, and H. Riegler, Impact of Negative Line Tension on the Shape of Nanometer-Size Sessile Droplets, Phys. Rev. Lett. **105**, 076103 (2010).

[28] L.-O. Heim and E. Bonaccurso, Measurement of line tension on droplets in the submicrometer range, Langmuir **29**, 14147 (2013).

[29] B. Zhao, S. Luo, E. Bonaccurso, G. K. Auernhammer, X. Deng, Z. Li, and L. Chen, Resolving the Apparent Line Tension of Sessile Droplets and Understanding its Sign Change at a Critical Wetting Angle, Phys. Rev. Lett. **123**, 094501 (2019).

[30] Y. A. Lei, T. Bykov, S. Yoo, and X. C. Zeng, The Tolman length: Is it positive or negative? J. Am. Chem. Soc. **127**, 15346 (2005).

[31] L. Schimmele, M. Napiórkowski, and S. Dietrich, Conceptual aspects of line tensions, J. Chem. Phys. **127**, 164715 (2007).

[32] L. Boinovich and A. Emelyanenko, The prediction of wettability of curved surfaces on the basis of the isotherms of the disjoining pressure, Colloids Surf. A **383**, 10 (2011).

[33] L. Boinovich and A. Emelyanenko, Wetting and surface forces, Adv. Colloid Interface Sci. **165**, 60 (2011).

[34] A. Rusanov, A. Shchekin, and D. Tatyanenko, The line tension and the generalized Young equation: The choice of dividing surface, Colloids Surf. A **250**, 263 (2004).

[35] B. Cheng and M. Ceriotti, Communication: Computing the Tolman length for solid-liquid interfaces, J. Chem. Phys. **148**, 231102 (2018).

[36] M. J. P. Nijmeijer, C. Bruin, A. B. van Woerkom, A. F. Bakker, and J. M. J. van Leeuwen, Molecular dynamics of the surface tension of a drop, J. Chem. Phys. **96**, 565 (1992).

[37] J. Gaydos and A. Neumann, The dependence of contact angles on drop size and line tension, J. Colloid Interface Sci. **120**, 76 (1987).

[38] D. Duncan, D. Li, J. Gaydos, and A. Neumann, Correlation of line tension and solid-liquid interfacial tension from the measurement of drop size dependence of contact angles, J. Colloid Interface Sci. **169**, 256 (1995).

[39] A. Amirfazli, D. Kwok, J. Gaydos, and A. Neumann, Line tension measurements through drop size dependence of contact angle, J. Colloid Interface Sci. **205**, 1 (1998).

[40] A. Amirfazli, D. Chatain, and A. Neumann, Drop size dependence of contact angles for liquid tin on silica surface: Line tension and its correlation with solid–liquid interfacial tension, Colloids Surf. A **142**, 183 (1998).

[41] J. Zhang, P. Wang, M. K. Borg, J. M. Reese, and D. Wen, A critical assessment of the line tension determined by the modified Young's equation, Phys. Fluids **30**, 082003 (2018).

[42] S. K. Das, S. A. Egorov, P. Virnau, D. Winter, and K. Binder, Do the contact angle and line tension of surface-attached droplets depend on the radius of curvature? J. Phys.: Condens. Matter **30**, 255001 (2018).

[43] M. Kanduč, L. Eixeres, S. Liese, and R. R. Netz, Generalized line tension of water nanodroplets, Phys. Rev. E **98**, 032804 (2018).

[44] A. A. Onischuk, P. A. Purtov, A. M. Baklanov, V. V. Karasev, and S. V. Vosel, Evaluation of surface tension and Tolman length as a function of droplet radius from experimental nucleation rate and supersaturation ratio: Metal vapor homogeneous nucleation, J. Chem. Phys. **124**, 014506 (2006).

[45] M. Toshev and M. Avramov, Van der Waals attraction forces and line tension, Colloids Surf., A **100**, 203 (1995).

[46] T. Chou, Geometry-Dependent Electrostatics Near Contact Lines, Phys. Rev. Lett. **87**, 106101 (2001).

[47] M. Iwamatsu, A generalized Young's equation to bridge a gap between the experimentally measured and the theoretically calculated line tensions, J. Adhes. Sci. Technol. **32**, 2305 (2018).

[48] N. Churaev and V. Sobolev, Prediction of contact angles on the basis of the Frumkin-Derjaguin approach, Adv. Colloid Interface Sci. **61**, 1 (1995).

[49] A. Moldovan, P.-M. Bota, T. D. Poteca, I. Boerasu, D. Bojin, D. Buzatu, and M. Enachescu, Scanning polarization force microscopy investigation of contact angle and disjoining pressure of glycerol and sulfuric acid on highly oriented pyrolytic graphite and aluminum, Eur. Phys. J.: Appl. Phys. **64**, 31302 (2013).

[50] L. Xu and M. Salmeron, Scanning polarization force microscopy study of the condensation and wetting properties of glycerol on mica, J. Phys. Chem. B **102**, 7210 (1998).

[51] F. Barberis and M. Capurro, Wetting in the nanoscale: A continuum mechanics approach, J. Colloid Interface Sci. **326**, 201 (2008).

[52] V. B. Svetovoy, I. Dević, J. H. Snoeijer, and D. Lohse, Effect of disjoining pressure on surface nanobubbles, Langmuir **32**, 11188 (2016).

[53] M. Rauscher and S. Dietrich, Nano-droplets on structured substrates, Soft Matter **5**, 2997 (2009).

[54] A. Oron, S. H. Davis, and S. G. Bankoff, Long-scale evolution of thin liquid films, Rev. Mod. Phys. **69**, 931 (1997).

[55] K. B. Glasner, Spreading of droplets under the influence of intermolecular forces, Phys. Fluids **15**, 1837 (2003).

[56] V. S. Ajaev, T. Gambaryan-Roisman, and P. Stephan, Static and dynamic contact angles of evaporating liquids on heated surfaces, J. Colloid Interface Sci. **342**, 550 (2010).

[57] H. Wong, S. Morris, and C. Radke, Three-dimensional menisci in polygonal capillaries, J. Colloid Interface Sci. **148**, 317 (1992).

[58] M. Gielok, M. Lopes, E. Bonaccurso, and T. Gambaryan-Roisman, Droplet on an elastic substrate: Finite element method coupled with lubrication approximation, Colloids Surf. A **521**, 13 (2017).

[59] B. Saramago, Thin liquid wetting films, Curr. Opin. Colloid Interface Sci. **15**, 330 (2010).

[60] J. A. Barrett and V. S. Ajaev, Modeling of moving liquid-vapor interfaces in the constrained vapor bubble system, Microgravity Sci. Tech. **31**, 685 (2019).

[61] N. V. Churaev, Surface Forces in Wetting Films, Colloid J. **65**, 263 (2003).

[62] N. Churaev and B. Derjaguin, Inclusion of structural forces in the theory of stability of colloids and films, J. Colloid Interface Sci. **103**, 542 (1985).

[63] T. Yi and H. Wong, Theory of slope-dependent disjoining pressure with application to Lennard–Jones liquid films, J. Colloid Interface Sci. **313**, 579 (2007).

[64] J. Kierzenka and L. F. Shampine, A BVP solver based on residual control and the maltab PSE, ACM Trans. Math. Softw. (TOMS) **27**, 299 (2001).

[65] See Supplemental Material at http://link.aps.org/supplemental/10.1103/PhysRevFluids.6.093603 for the supplemental figures and discussion of the findings of Sec. IV (B) in the context of the soft wetting.

[66] N. Churaev, Wetting films and wetting, Rev. Phys. Appl. **23**, 975 (1988).

[67] S. G. Kazakova, E. S. Pisanova, A. Angelopoulos, and T. Fildisis, Some Applications of the Lambert W-Function to Theoretical Physics Education, AIP Conf. Proc. **1203**, 1354 (2010).

[68] R. Giro, P. W. Bryant, M. Engel, R. F. Neumann, and M. B. Steiner, Adsorption energy as a metric for wettability at the nanoscale, Sci. Rep. **7**, 46317 (2017).

[69] R. Iqbal, A. Matsumoto, A. Sudeepthi, A. Q. Shen, and A. K. Sen, Substrate stiffness affects particle distribution pattern in a drying suspension droplet, Appl. Phys. Lett. **114**, 253701 (2019).

[70] M. Iwamatsu, The characterization of wettability of substrates by liquid nanodrops, Colloids Surf. A **420**, 109 (2013).

[71] G. F. Teletzke, H. T. Davis, and L. Scriven, Wetting hydrodynamics, Rev. Phys. Appl. **23**, 989 (1988).

[72] L. R. White, The contact angle on an elastic substrate. 1. The role of disjoining pressure in the surface mechanics, J. Colloid Interface Sci. **258**, 82 (2003).

[73] S. Das, A. Marchand, B. Andreotti, and J. H. Snoeijer, Elastic deformation due to tangential capillary forces, Phys. Fluids **23**, 072006 (2011).

[74] J. Dervaux and L. Limat, Contact lines on soft solids with uniform surface tension: Analytical solutions and double transition for increasing deformability, Proc. R. Soc. A **471**, 20140813 (2015).

[75] N. Bergemann, A. Juel, and M. Heil, Viscous drops on a layer of the same fluid: From sinking, wedging and spreading to their long-time evolution, J. Fluid Mech. **843**, 1 (2018).

[76] R. W. Style, R. Boltyanskiy, Y. Che, J. S. Wettlaufer, L. A. Wilen, and E. R. Dufresne, Universal Deformation of Soft Substrates Near a Contact Line and the Direct Measurement of Solid Surface Stresses, Phys. Rev. Lett. **110**, 066103 (2013).

[77] J. B. Bostwick, M. Shearer, and K. E. Daniels, Elastocapillary deformations on partially-wetting substrates: Rival contact-line models, Soft Matter **10**, 7361 (2014).

[78] R. Pericet-Camara, G. K. Auernhammer, K. Koynov, S. Lorenzoni, R. Raiteri, and E. Bonaccurso, Solid-supported thin elastomer films deformed by microdrops, Soft Matter **5**, 3611 (2009).

[79] M. Zhao, Wetting on soft gels, Ph.D. thesis, PSL Research University, Paris, 2017.

[80] G. Ahmed, N. Koursari, A. Trybala, and V. M. Starov, Sessile droplets on deformable substrates, Colloids Interfaces **2**, 56 (2018).

[81] M. Ghosh and K. J. Stebe, Spreading and retraction as a function of drop size, Adv. Colloid Interface Sci. **161**, 61 (2010).

[82] D. R. Heine, G. S. Grest, and E. B. Webb, Spreading dynamics of polymer nanodroplets, Phys. Rev. E **68**, 061603 (2003).

[83] Q. Wu and H. Wong, A slope-dependent disjoining pressure for non-zero contact angles, J. Fluid Mech. **506**, 157 (2004).